



Current Trends in Preclinical PET System Design

Craig S. Levin, PhD^{a,*}, Habib Zaidi, PhD, PD^b

- Why small-animal PET?
- Brief history of preclinical PET
- Currently available small-animal PET systems
- Challenges to improving the performance of small-animal PET systems
 - Photon sensitivity*
 - Spatial resolution*
 - Contrast and contrast resolution*
- Promising future technologies for small-animal PET
 - New strategies to increase the photon sensitivity*

New strategies to enable increased spatial resolution

New strategies to enhance contrast and contrast resolution

- Instrumentation and algorithms for combining PET with other imaging modalities

Software-based approaches

Hardware-based approaches

- Quantification of small-animal PET data
- Biomedical applications of preclinical PET
- Summary and future directions
- Acknowledgments
- References

Why small-animal PET?

The last 2 decades of biomedical research have seen a rapid expansion in the use of small-animal models for studying disease. During this period the need evolved to perform these animal-model studies *in vivo*, that is in living, intact subjects, so the disease could be studied in its true, natural biologic state, including regulatory and feedback mechanisms such as the immune and circulatory systems that are not present in *in vitro* biologic

studies. Furthermore, because *in vivo* imaging enables repeated, longitudinal, nondestructive studies, the same animal can be used as its own control in distinct stages of a study, increasing the accuracy of results and improving the efficiency of animal use. Finally, because *in vivo* imaging allows rapid and accurate assessment of disease progress or regression before and after novel treatments are introduced, this tool for biologic study offers the attractive possibility of reducing the time required to bring promising new pharmaceuticals or

This work was supported by grants #R01CA119056, R01EB120474, R33 EB003283, and R21 CA098691 from the National Institutes of Health, 12IB-0092 from the California Breast Cancer Research Program, and graduate research fellowships from the Stanford University Bio-X Graduate Program, the Society of Nuclear Medicine, the NVIDIA Corporation Research Fellowship Program, and grant #SNSF 3100A0-116547 from the Swiss National Foundation.

^a Molecular Imaging Program, Division of Nuclear Medicine, Department of Radiology, Stanford University School of Medicine, 300 Pasteur Drive, MC 5128, Alway Building, Room M001, Stanford, CA 94305-5128, USA

^b Division of Nuclear Medicine, Geneva University Hospital, CH-1211 Geneva, Switzerland

* Corresponding author.

E-mail address: cslevin@stanford.edu (C.S. Levin).

therapeutic agents to the clinic. Thus, small-animal imaging systems are becoming popular tools for drug discovery, and, in addition to programs developing at academic centers, small-animal imaging laboratories are becoming prevalent in the pharmaceutical and biotechnology industries [1–28].

PET has several strengths as a small-animal (ie, preclinical) imaging modality [29]. First, like other biologic imaging techniques such as optical imaging, PET can be used to study the cellular and molecular processes associated with disease in live animals. Unlike optical imaging, however, PET can probe subtle molecular signals (low probe concentrations) deep within tissue with high spatial resolution and contrast and thus provide quantitatively accurate data about the spatial and temporal biodistribution of the probe. The molecular probes typically are low-mass, biologically relevant molecules and thus are unlikely to perturb the natural states of cells and tissues. Finally, because PET is already a clinical standard of care, preclinical discoveries and developments are more likely to translate into the clinic.

PET now is used regularly in small-animal research to study the molecular bases of disease noninvasively and to guide the development of novel molecular-based treatments [1–28]. Several new molecular probes labeled with positron-emitting radionuclides and associated PET imaging assays are under development to target, detect, visualize, and quantify various extra- and intracellular molecules and processes associated with diseases such as cancer, heart disease, and neurologic disorders [1–28]. Thus there is a continuing need to improve “sensitivity” to detect the subtle signatures associated with these new molecular targets and processes. The authors define the “molecular sensitivity” of a molecular imaging modality as its ability to detect, visualize, and accurately quantify low concentrations of a molecular probe interacting with a target on or within the cells of a living subject. The molecular sensitivity depends on a combination of the probe, the physiology of the delivery process, and cellular function that determine its preferential accumulation at the target. This sensitivity also depends on the performance capabilities of the imaging system that determine how small a signal can be detected above background and how accurately that signal can be measured. This article discusses the current trends in preclinical PET system design that strive to increase molecular sensitivity, with a focus on systems designed for rodent imaging.

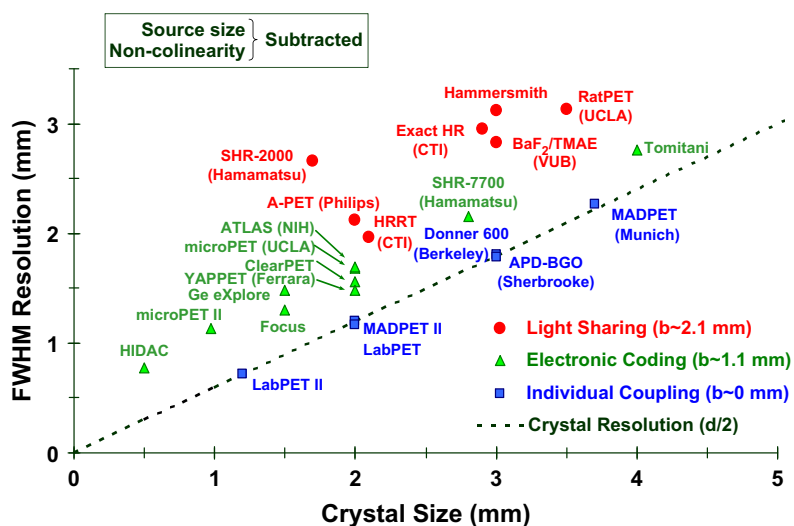
Brief history of preclinical PET

Some of the most notable early uses of clinical PET in imaging animal models of disease were in

neurologic studies in nonhuman primates [30,31] and dogs [32]. The need to resolve very small structures in the brains of smaller species of monkeys resulted in the development of a few specialized systems [33,34]. During the past 2 to 3 decades, however, efforts to develop efficient animal models of disease for understanding mammalian biology have concentrated on rodents, and in particular mice [35]. The mouse genome is very similar to that of humans and is relatively easy to manipulate. Mice are small, inexpensive, and have a rapid reproductive rate and a short life span [36,37]. Rats usually are the preferred species for neuroscience and neurosurgery models, because their brains are approximately five times larger (and thus easier to work with), and there is a strong history of rat brain anatomy and function studies. The first PET system designed and dedicated to imaging rodents was developed by Hammersmith Hospital (London, UK) in collaboration with CTI PET Systems, Inc. (Knoxville, Tennessee) [38]. This system comprised 16 block detectors arranged into a ring 11.5 cm in diameter with a 5-cm axial field-of-view (FoV). Each detector comprised an 8×7 array of $3.5 \times 6.0 \times 30\text{-mm}^3$ bismuth germanate (BGO) scintillation crystals. The measured spatial resolution at the system center was 2.4 mm in the transaxial plane and 4.6 mm along the axial direction. The absolute photon sensitivity of the scanner at the center of the FoV was 4.3% using a 250- to 750-keV energy window. Main shortcomings of this system were its relatively coarse resolution, large angular gaps between detectors which led to reconstructed image artifacts, and the non-uniform spatial resolution versus radial position (caused by variations in the depth of the 511-keV photon interaction). The system produced useful data despite these inadequacies and spawned the development of a new generation of small-animal PET systems.

Currently available small-animal PET systems

To clearly visualize and accurately quantify the biodistribution of a PET tracer in small structures within rodents, especially mice, requires special high-resolution PET systems. During the past decade substantial research and energy have been devoted to the development of preclinical PET systems for rodent research. This work has resulted in the development of numerous research prototypes [39–46] as well as commercially available [47–53] small-animal PET systems (Fig. 1). With the exception of one commercially available gas-based multiwire proportional counter (MWPC) design, nearly all small-animal PET systems use variations of the same basic position-sensitive annihilation photon detector concept, which essentially is



scintillation crystals to independent photodetectors allows the spatial resolution to be improved by eliminating the degradation caused by crystal encoding. (Courtesy of Dr. R. Lecomte, University of Sherbrooke, Sherbrooke, Ontario, Canada.)

a miniature version of that used in clinical PET system designs. The system is built from detector modules arranged into a ring. Each module comprises arrays of long, thin scintillation crystal rods with their small ends coupled to a position-sensitive array of photodetectors. Each crystal rod is covered with a very thin reflector, except for the end face coupled to the photodetector, so that each is optically isolated from its neighbors. An incoming photon that interacts in one of the crystal rods creates a small flash of light. The light pulse reflects off the crystal faces and exits the end of the crystal rod coupled to the photodetectors. The photodetectors collect and convert the exiting light into electronic pulses, which are amplified and processed to estimate the incoming interaction location, total energy deposited, and arrival time of each incoming annihilation photon. The photodetectors almost always are photomultiplier tubes (PMT) and, for small animal PET, typically position-sensitive PMTs (PSPMT), which contain an array of charge-collecting anodes within a single evacuated vacuum tube. The signals induced on the anodes can be used to localize the scintillation light flash to within a few millimeters or less. A variation of the basic scintillation detector uses semiconductor photodetectors, such as avalanche photodiodes (APDs), instead of PMTs to read out the scintillation light.

The currently commercially available small-animal PET system designs are all offshoots from systems developed for academic research, and nearly all are variations of the basic scintillation detector system described. For example, a technology developed at the University of California, Los Angeles (UCLA) in the late 1990s [40] was transferred to what has become the Siemens microPET product line (Siemens Preclinical Solutions, Knoxville,

Fig. 1. Intrinsic resolution of PET scanners (ignoring contributions of positron range and with source size and annihilation photon non-collinearity deconvolved) versus individual crystal size. The dashed line represents the geometric resolution of the detectors, which is roughly half the detector pixel width. The difference between measured spatial resolutions and this line are attributed to the resolution degradation caused by positron range effects as well as decoding of the crystal of interaction for those “multiplexed” designs that implement light sharing or electronic coding in their detector designs. A one-to-one coupling of individual

Tennessee) [47]. The detector module design uses an optical fiber interface between a lutetium-oxyorthosilicate (LSO) scintillation crystal array and a multianode PSPMT to enable a high inter-module packing fraction. The current-generation system, the Inveon, uses block modules comprising 20×20 arrays of $1.5 \times 1.5 \times 10$ mm³ LSO crystals, arranged in a 16.1 cm diameter ring, with a bore 12 cm in diameter and a 10-cm transaxial and 12.7-cm axial FoV. The spatial resolution and photon sensitivity are 1.4 mm full-width-at-half-maximum (FWHM) and 10% (100-keV threshold), respectively, respectively, at the system center.

Work at the National Institutes of Health was translated to Suinsa (Madrid, Spain) [41] and became what is now known as the GE eXplore Vista PET system (GE/Suinsa, Madrid, Spain) [48]. This design uses a two-layer scintillation crystal array or “phoswich” to allow coarse estimation of photon depth of interaction (DOI). Each layer is made from a different type of scintillation crystal (lutetium-yttrium-oxyorthosilicate [LYSO] or gadolinium orthosilicate [GSO] with a different scintillation light decay constant. Pulse-shape discrimination methods are used to determine which array layer was hit by an incoming photon. The system has two rings of 6084 LYSO-GSO crystals arranged into modules, each containing 13×13 arrays of $1.5 \times 1.5 \times 15$ -mm³ LYSO-GSO pairs. The detector diameter is 11.8 cm, with a 6-cm transaxial FoV and a 4.6-cm axial FoV. The reconstructed spatial resolution is 1.6 mm FWHM at the center with a 4% absolute photon sensitivity (250-keV threshold) [54].

The detector scheme developed at University of Pennsylvania [42,55] was incorporated in the Philips Mosaic small-animal PET system (Philips

Medical Systems, Andover, Massachusetts) [49]. Unlike other scintillation crystal designs, the Mosaic is not partitioned into individual block modules. The system uses just under 17,000 discrete $2 \times 2 \times 10\text{-mm}^3$ GSO crystals coupled through a single large annular light diffuser to a bank of standard PMTs, with a bore 21 cm in diameter, a 12.8-cm transaxial FoV, and an 11.6-cm axial FoV. The reconstructed spatial resolution ranges between 2.7 mm FWHM at the center and 3.2 mm FWHM at a radial offset of 45 mm from the center with an absolute photon sensitivity of 0.65% (410-keV threshold) [56].

A research concept from the University of Texas [43] has been incorporated into a system offered by Gamma Medica-Ideas (Northridge, California) [50]. The system uses BGO scintillation crystals with a light-sharing technology that allows them to be read out by standard PMTs. The edge crystals of each module are trapezoidal to promote high inter-detector module crystal packing fraction (reduced gaps between modules). At the system center the specified spatial resolution is 1.5 mm FWHM with a photon sensitivity of 10%.

A development at the University of Sherbrooke in Quebec, Canada [57] was transferred to Advanced Molecular Imaging, Inc. (Sherbrooke, Quebec, Canada) and more recently to Gamma Medica-Ideas [50]. The basic detector design uses an array of two different scintillation crystals (LYSO and lutetium-gadolinium-oxyorthosilicate) with different decay times coupled to a single APD device. Pulse-shape discrimination allows the use of only one readout channel to identify which of the two crystals has been hit by an incoming photon. The resulting system has a detector ring 15.6 cm in diameter with an aperture 11 cm in diameter and either a 3.7- or 7.5-cm axial FoV with 1536 or 3072 APDs, respectively. At the system center the specified spatial resolution is 0.9 mm FWHM with a photon sensitivity of 2%–4%, depending on the axial FoV.

The yttrium-aluminum-perovskite (YAP)-PET system [51] is an off-shoot from the Universities of Ferrara and Pisa, in Italy [45]. The system comprises four rotating heads spaced 15 cm apart, each with an active area of $4 \times 4 \text{ cm}^2$, containing a 20×20 array of $2 \times 2 \times 3\text{-mm}^3$ optically isolated YAP crystals coupled to PSPMTs, forming a 4-cm transaxial and axial FoV. The reconstructed spatial resolution and absolute photon sensitivity are 1.8 mm FWHM and 1.7% (50-keV threshold) for a centered point source, respectively.

The ClearPET LYSO/LuYAP phoswich scanner [52] is a technology transfer incorporating ideas developed within the ClearPET group [46] of the Crystal Clear Collaboration, a scintillation crystal research organization based at CERN, an

international particle physics laboratory located in Geneva, Switzerland. The system has two adjustable detector diameters, 13.5 and 28.5 cm, with an open gantry space of 12.5 and 22.0 cm, respectively. The phoswich detectors comprise two layers of $2 \times 2 \times 10\text{-mm}^3$ crystals of LYSO and lutetium orthoaluminate (LuYAP) coupled to PSPMTs. Because of significant gaps between the detectors, the system rotates around the subject to enable full angular sampling. At the system center, the resolution is 1.3 mm, and the absolute photon sensitivity is 3.8%.

The Oxford Positron Systems (Wadsley Grove, UK) high-density avalanche chamber (HIDAC) PET system [53] is a culmination of years of high-resolution gas MWPC imaging system developments at CERN that were modified and refined for small-animal imaging [58]. In this position-sensitive gas ionization chamber, the annihilation photons are converted by lead cathode plates into electrons, which subsequently are detected and localized by collecting the ionization generated as they drift and avalanche in the gas. The lead cathode plates are formed from layers of laminated lead containing interleaved insulated sheets, mechanically drilled with approximately 200,000 holes, each 0.4 mm in diameter, each of which acts as an independent detector element. The hole pitch, approximately 0.5 mm, limits the intrinsic resolution. The quad-HIDAC consists of four large rotating heads, each with eight HIDAC detector layers with an active area of $17 \times 28 \text{ cm}^2$ and with a head separation of 17 cm. These layers provide information about the photon interaction depth. The transaxial and axial FoVs are 17 cm and 28 cm, respectively. The reconstructed resolution is 1.0 mm throughout the FoV (not just at the center, which is another distinguishing feature of the HIDAC technology), and the absolute sensitivity is 1.8% for an effective 200-keV threshold. Two variants for this technology are commercially available comprising 16 [59] and 32 modules [60].

Challenges to improving the performance of small-animal PET systems

Of all the photon-sensing fields, PET imposes perhaps the most stringent requirements on detector capabilities. As discussed earlier, nearly all the available small-animal PET systems are built from crystals, and thus crystals are the technologic focus of this section. The detector crystals comprise relatively high atomic number (Z), high-density materials for a high probability of the photoelectric effect and high intrinsic efficiency in the detection of the 511-keV photons. Typically, high-quality inorganic scintillation crystals are used (Table 1). The crystals absorb the 511-keV photons and

Table 1: Some properties of cadmium-zinc-telluride and common scintillation crystals used in PET

Crystal name	Formula	Effective atomic number Z_{eff}	1/e Length density ρ at 511 keV (g/cm ³)	Total linear absorption coefficient at 511 keV (cm ⁻¹)	Compton scatter fraction μ_c/μ at 511 keV (cm ⁻¹)	Average		Decay time (ns)	Refractive index n	Peak emission wavelength (nm)
						Photoelectric absorption fraction μ_p/μ at 511 keV	Number of electrons ^a created per MeV absorbed			
CZT	Cd _{0.9} Zn _{0.1} Te	48	5.81	2.00	0.500	0.820	0.180	200,000	N/A	N/A
LSO	Lu ₂ (SiO ₄)O:Ce	66	7.40	1.13	0.869	0.620	0.323	4400	1.82	420
GSO	Gd ₂ (SiO ₄)O:Ce	59	6.71	1.40	0.704	0.700	0.249	1400	1.85	440
BGO	Bi ₄ (GeO ₄) ₃	75	7.13	1.06	0.966	0.510	0.397	1200	2.15	300
										480

Abbreviations: BGO, bismuth germanate; CZT, cadmium-zinc-telluride; GSO, gadolinium orthosilicate; LSO, lutetium-oxyorthosilicate.

^a A PMT quantum efficiency of 20% was assumed for LSO, GSO, and BGO. Photoelectrons created at photomultiplier tube photocathodes are listed.

convert them into robust electronic signals, which must be processed one at a time and used to determine precisely the incoming position, energy, and arrival time of each incoming photon. The performance of a small-animal PET system can be improved by enhancing important performance parameters of the detector system, such as photon sensitivity, spatial resolution, and contrast resolution. This section describes some of the challenges involved and solutions that have been implemented in existing systems. The subsequent section describes what the authors believe are promising technologies for the future.

Photon sensitivity

Photon sensitivity is defined here as the fraction of coincident annihilation photon pairs emitted from a source that is detected and counted in the study. This fraction should be as high as possible to achieve an acceptable signal-to-noise ratio (SNR) for high-spatial-resolution reconstructed images. Better statistical quality of the data also enhances the ability to differentiate and quantify a subtle signal in the presence of significant background counts. The photon sensitivity is determined by the geometric efficiency, which depends on the solid angle coverage of the detector, and on the intrinsic detection efficiency, which depends on the effective Z, density, thickness, and packing fraction of the crystal as well as on the energy and coincidence time window settings.

System geometric efficiency

The system geometric efficiency, g (ie, the solid angle coverage) is the probability that an emitted photon is directed toward the detector gantry. The system photon sensitivity varies linearly with g . One way to improve the geometric efficiency is to reduce the system diameter, which essentially brings the detector system closer to the photon source. In that case, however, more photons will enter the detector crystals at large oblique angles, which can cause substantial parallax positioning errors and associated spatial resolution loss resulting from 511-keV photon penetration unless a method for assigning the photon interaction depth is implemented. Another approach to increase geometric efficiency is to increase the axial extent of the scintillation detectors, covering more solid angle about the subject but also increasing system cost substantially. The GE eXplore Vista dual ring system (GE Healthcare/Suinsa, Madrid, Spain) [48], for example, incorporates a modest 7.5-mm DOI resolution enabling a small detector diameter of just under 12 cm while controlling DOI parallax errors. The axial FoV is only 4.6 cm, however, which offsets the potential improvements in photon

sensitivity available with the smaller ring diameter. Geometric efficiency for small-animal PET systems is enhanced further in that all available systems acquire data in the three-dimensional (3D) mode, which means all photon coincidences between any two crystal elements are accepted into the system and no inter-ring septa are present.

Crystal length (thickness)

Because the intrinsic efficiency in detecting coincidence photons for any two crystal element pairs of linear attenuation coefficient μ varies with crystal element length, l , by the square of an exponential [$\epsilon \sim (1-e^{-\mu l})^2$], it is clear that the effective crystal length should be as large as possible. In the standard design for a scintillation crystal detector used in high-resolution PET, however, the efficiency of light collection decreases and the likelihood of inter-crystal scatter and photon penetration increase for longer crystal elements. Thus, many small-animal PET systems use crystals that are only approximately 1 cm long. Building a PET system with LSO crystal lengths of only 1 cm affects the intrinsic coincident photon detection efficiency by a factor of 0.34 [$\epsilon = (1-e^{-\mu x})^2$; $\mu_{\text{LSO}} = 0.87 \text{ cm}^{-1}$; $x = 1 \text{ cm}$]. This relatively low intrinsic detection efficiency factor contributes significantly to the relatively low overall photon sensitivity (approximately a few percent) achieved with currently available high-resolution PET systems [61].

Crystal packing fraction

The crystal packing fraction, P , is defined as the fraction of the area that is occupied by scintillation crystal as seen by an incoming photon directed at the detector gantry. A high packing fraction means that the gaps allowing incoming photons to escape undetected are very small. For imaging coincident photons in PET, the intrinsic photon detection efficiency also varies as the square of the packing fraction, $\epsilon \sim P^2$. The crystal packing fraction is reduced by the presence of dead gaps between detector modules. Typically the detector modules in a PET system are rectangular. Arranging rectangular detectors into a cylinder produces wedge-shaped gaps between detectors through which photons can escape (Fig. 2). To mitigate this problem, the Gamma Medica-Ideas X-PET design incorporates wedge-shaped crystals at the edge of each module to fill these gaps [50]. The packing fraction is reduced by dead area introduced by the mechanical package that houses the photodetector (eg, the PSPMT) for each detector module. The effect of dead area in the PSPMT housing on packing fraction can be mitigated using fiberoptic coupling between the scintillation crystal array and the PSPMT, which is implemented in the Siemens designs [47], but the additional fiberoptic coupling reduces light collection. The Philips

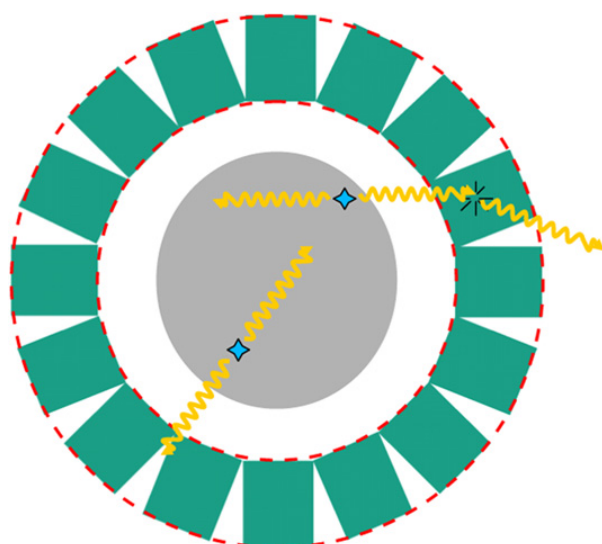


Fig. 2. The standard configuration of rectangular block detectors arranged into a cylindrical system configuration yields many intermodule wedge-shaped gaps that provide a path for photons to escape. The probability for crystal-scattered photons to escape is high (example shown). The escape of crystal-scattered photons plays a larger role in degrading system photon sensitivity than does the penetration of nonscattered photons (example shown). (Adapted from Habte F, Foudray AMK, Olcott PD, et al. Effects of system geometry and other physical factors on photon sensitivity of high-resolution positron emission tomography. Phys Med Biol 2007; 52:3756; with permission.)

Mosaic design [49] incorporates a light diffuser between the scintillator arrays and the standard PMTs used in their design and uses standard gamma camera light-sharing concepts to mitigate the photodetector dead area. The crystal packing fraction also is affected by the presence of intercrystal reflectors within a module, which should be as thin as possible while still providing optical isolation of the individual scintillation crystals. For example, the state-of-the-art Siemens microPET systems use an intercrystal reflector that yields an intercrystal gap of approximately 75 microns within a module.

Spatial resolution

To date, no PET system has achieved the fundamental spatial-resolution potential inherent to PET. The physical limit of spatial resolution is determined ultimately by a convolution of three blurring factors: positron range, annihilation photon non-collinearity, and intrinsic detector resolution [63]. For central points between two coincident detector elements, the intrinsic detector spatial resolution is approximately one half the detector element size. The blurring component caused by positron range is shift invariant within the system but depends on the energy range of the emitted positron and the tissue traversed. The effect of photon

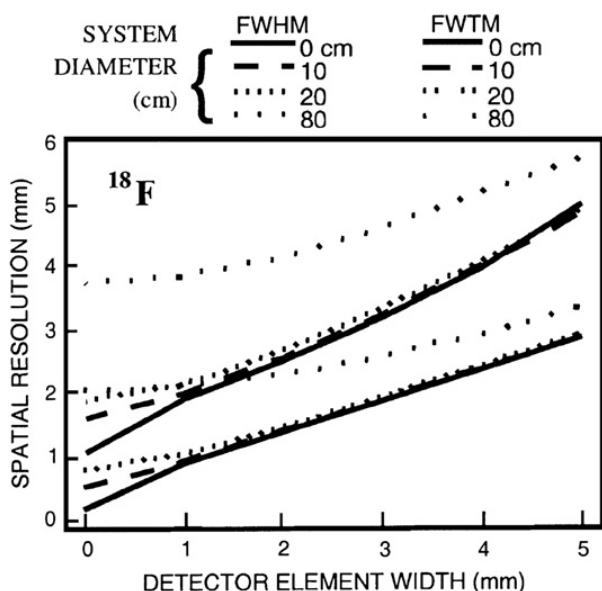


Fig. 3. Calculated ^{18}F point source spatial resolution (FWHM and FWTM) limit for PET from a convolution of positron range, photon acollinearity, and detector contributions as a function of detector pixel size and the system detector diameter. In theory, for a 1-mm detector pixel and a detector separation of less than 20 cm, adequate statistics, and sufficient sampling, a FWHM spatial resolution of less than 1 mm is possible. (Adapted from Levin CS, Hoffman EJ. Calculation of positron range and its effect on the fundamental limit of positron emission tomography system spatial resolution. *Phys Med Biol* 1999;44:796; with permission.)

acollinearity on spatial resolution depends on the system diameter. **Fig. 3** shows a plot of the calculated spatial resolution (FWHM and full width at tenth maximum [FWTM], respectively) for a point source of ^{18}F in water-equivalent tissue determined by these three blurring factors for various system diameters as a function of detector pixel size [63]. In principle, approximately 750- μm FWHM

(submillimeter) resolution is attainable with 1-mm detector pixellation and a system diameter of 20 cm or less, provided there are adequate counts to reconstruct at that desired resolution with acceptable SNR [64]. It is clear from this figure that to increase PET spatial resolution, one should build a system with crystal pixels and a system diameter (or distance between opposing detectors) as small as possible, but these goals present several challenges.

Complex and expensive assembly

Higher-spatial-resolution PET data are achieved by using smaller detector elements to provide finer sampling of the biodistribution of interest. A major challenge of manufacturing PET detectors with smaller (< 2 mm wide) scintillation crystal elements is that cutting, surface treatments, and assembling crystals to make arrays (**Fig. 4**) are complex and costly processes, and special system-dependent processing schemes must be developed [65,66].

Less light signal is available from small crystals

For high detection efficiency, the crystals should be thick (eg, > 2 cm), but for high spatial localization of the incoming photons, a high degree of crystal segmentation/pixellation (eg, < 2 mm width) is required. This long but very narrow aspect ratio for the individual scintillation crystal elements compromises the efficiency of scintillation light collection [67,68]. The longer and narrower the crystal element, the less light collected is from the small end. If the resulting light signal in each crystal is above the corresponding photodetector noise level, it still is possible to achieve high-resolution PET. It is clear, however, that this scenario is not desirable, because a weak scintillation light signal ultimately degrades energy and temporal resolution, affects energy and window settings, and limits the degree of

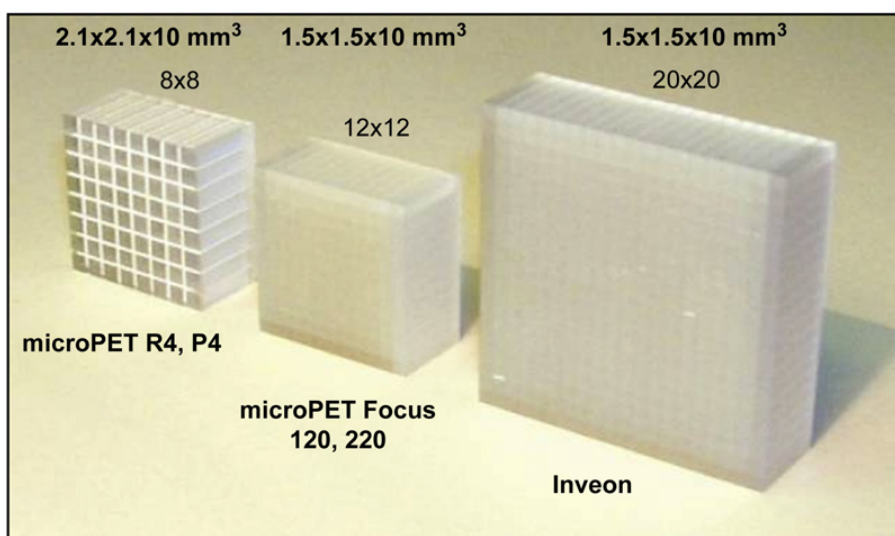


Fig. 4. Examples of arrays (8×8 , 12×12 , and 20×20) of discrete LSO scintillation crystals pixels used in three successive generations of microPET systems. In these system designs, each array is coupled to a position-sensitive photomultiplier tube through fiberoptic coupling. Individual crystal element dimensions are shown above each array. (Courtesy of Robert Nutt, Siemens Pre-clinical Solutions, Knoxville, TN.)

crystal position decoding in most detector designs. Any fiber coupling introduced between scintillator and light detector causes further light loss. Modest improvements in light collection can be made by treating the crystal side faces (eg, by polishing or etching) to enhance total internal reflection [67,68].

To provide a more favorable aspect ratio with moderate light collection efficiency, PET systems built to date with resolutions of 2 mm or less [40,42–44,46,47,49,50,52,53,65,66] use relatively short crystals approximately 10 mm in length (see Fig. 4). Although this short-crystal design provides decent light collection efficiency, it severely compromises the intrinsic efficiency of 511-keV photon detection, as described in the previous section.

Photon penetration and parallax blurring effects

Because 511-keV photons are highly penetrating, it becomes impossible as the crystal pixels become narrower to confine the photon interactions to only one crystal element. Fig. 5 shows results from Monte Carlo simulations of 511-keV photons entering obliquely (at 20° with respect to the normal) into an array of $1 \times 1 \times 10\text{-mm}^3$ LSO crystal pixels [68]. The line of dense interactions in the array corresponds to the line of entry. For this configuration, 84% of the detected incoming photons interact outside the crystal of entrance. Most PET systems comprise a cylindrical arrangement of

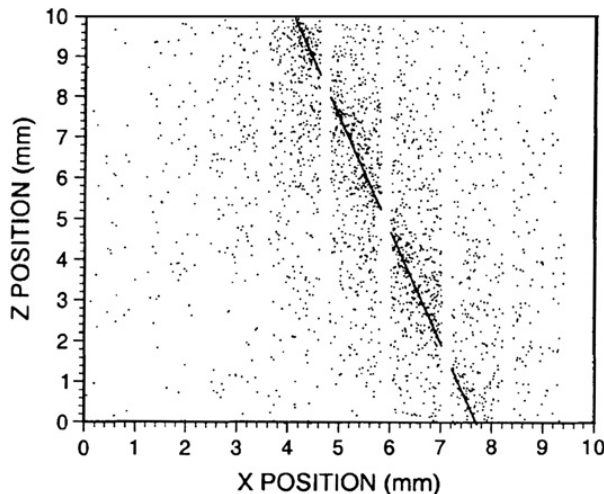


Fig. 5. Distribution of interaction vertices in an 8×8 array of $1 \times 1 \times 10\text{-mm}^3$ LSO crystals for a narrow beam of 511 keV photons entering at a 20° incident angle with respect to the normal onto a center crystal as calculated by Monte Carlo simulation. Views of the distribution projected from the side of the array are shown. A total of 20,000 incident photons were simulated. (Adapted from Levin CS. Design of a high-resolution and high-sensitivity scintillation crystal array for PET with nearly complete light collection. IEEE Trans Nucl Sci 2002;49:2241; with permission. Copyright © 2002 IEEE.)

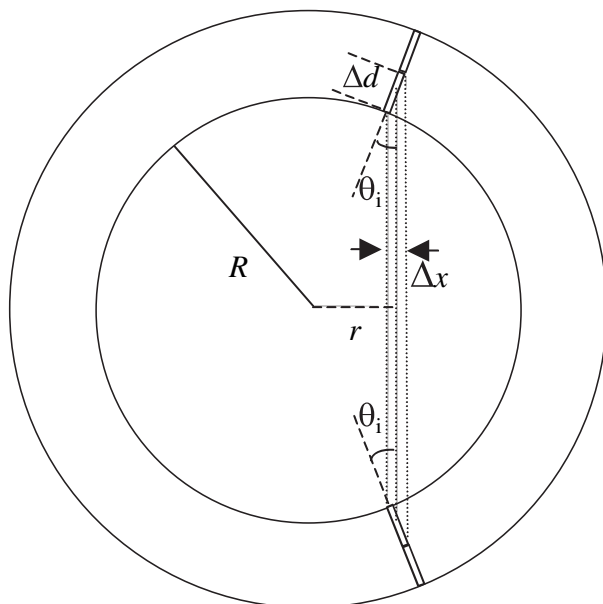


Fig. 6. Depiction of the radial resolution blurring caused by variation in interaction depth for coincident photons emitted from a point source located at radial coordinate r entering obliquely into two isolated crystal elements. The radial resolution blurring, Δx , is mitigated by using detectors that can measure photon interaction depth precisely.

such arrays (Fig. 6). The substantial crystal penetration of 511-keV photons leads to non-uniform spatial resolution as a function of radial position within the scanner. For a small-diameter PET system with closely spaced detectors, on average more photons will enter and be absorbed in the scintillation crystal at oblique rather than normal angles for a given imaging subject. In this case photons will tend to interact at depth in crystals behind the first crystal traversed, causing a parallax error [69]. Because of the variation in photon interaction depth within the crystals for obliquely entering photons, blurring of the radial component of the spatial resolution increases linearly with radial position (see Fig. 6). The precision with which photon interaction depth can be measured, referred to as the "interaction depth resolution," impacts the degree of radial resolution blurring. As shown in Fig. 6, the distance (r) from the tomograph center to the particular line-of-response (LoR) chord formed between two crystal elements that corresponds to photons incident at angle θ_i that interact at the center of isolated crystal segments of length Δd of a system of radius R is given by:

$$r = (R + (\Delta d/2)) \sin \theta_i \quad (1)$$

An expression for the radial resolution blurring in the transaxial plane for photons incident at angle θ_i that interact in an isolated detector with interaction depth resolution Δd can be determined by assuming that the entire length of that crystal segment Δd is uniformly radiated by these oblique photons.

The radial resolution blurring for photons interacting in two isolated detectors in coincidence is approximately given by one half the effective width of the detector seen (see Fig. 6):

$$\begin{aligned}\Delta r \approx \Delta x/2 &= (\Delta d/2) \sin\theta_i \text{ (FWHM)} \\ &= (\Delta d/2) r/[R+(\Delta d/2)] \\ &= r/[(D/\Delta d)+1]\end{aligned}\quad (2)$$

where D is the system detector diameter. Note at the center ($r = 0$) there is no radial blurring from photon penetration regardless of the system diameter or degree of photon interaction depth resolution. For a typical clinical system, $D = 80$ cm and $\Delta d = 2$ cm (crystals 20 mm long with interaction depth resolution), at $r = 10$ cm from the center, from equation 2, the radial blurring contribution from photon penetration is $\Delta r = 2.4$ mm FWHM, a radial resolution blurring contribution that is 40% (2.4/6) of the typical value of 6 mm FWHM measured at the center. On the other hand, for a typical small-animal PET system, $D = 16$ cm and $\Delta d = 1$ cm, and at $r = 2$ cm, the effective radius of a typical mouse, $\Delta r = 1.1$ mm, is 60% of the typical 2 mm FWHM resolution measured at the center. For the GE eXplore Vista system, $D = 11.8$ cm, $\Delta d = 0.75$ cm, and thus at $r = 2$ cm, $\Delta r = 1.2$ mm, which is 75% of the 1.6-mm FWHM resolution quoted at the center. Note that the total spatial resolution at a given radial location is the convolution of the parallax blurring factor Δr and the resolution value at the center determined by the other blurring factors.

Lower photon counts per crystal element

The smaller the crystal element, the fewer photon counts are placed in that crystal, and hence the lower is the SNR per crystal. Thus, to achieve the desired improved spatial resolution in terms of SNR in reconstructed images [64], the system photon sensitivity must be increased substantially.

Image reconstruction complexity

PET data with higher spatial resolution are achieved by using smaller detector elements to provide finer sampling of the imaged volume. However robust, statistical-based image reconstruction algorithms, ideally with spatially variant response models, are also needed, to recover the desired potential spatial resolution with an acceptable SNR [70]. Fully 3D iterative reconstruction with spatially varying models has been shown to increase the image quality of these systems [71]. Furthermore, using detectors capable of measuring photon DOI, one can bring the detectors closer together for increased photon sensitivity, and hence enhanced image SNR, while mitigating parallax errors that blur spatial resolution

[72]. As the result of these advances, the number of LoRs or, alternately, the number of non-zero elements in the system response matrix, continues to increase by orders of magnitude (Fig. 7) [73].

The computational cost of fully 3D PET image reconstruction, especially with spatially varying system response models, is daunting. As the number of LoRs and reconstructed image resolution continues to increase, the demand for computation power and memory storage for high-resolution PET image reconstruction continues to explode, in many cases outpacing the advances in processor performance and memory capacity. Algorithms whose complexity does not depend on the number of LoRs are attractive to process efficiently the extremely sparse data generated by high-resolution PET systems with minimal memory storage requirements. Three classes of algorithms can help mitigate the problem of the sparseness of the high-resolution 3D PET data: reduced-resolution sinogram binning, 3D to two-dimensional(2D) rebinning, and list-mode processing. The process of binning events into a lower-resolution sinogram may result in a loss of spatial resolution, because the counts associated with a number of neighboring lines in space that are individually resolvable by the detector system will be accumulated together in the same histogram bin, possibly undersampling the signal [74]. On the other hand, 3D sinograms that provide sampling of at least twice the Nyquist frequency can be too sparse. Thus, sinogram-binning approaches to deal with the sparseness of the data can lead to a tradeoff between desired reconstructed spatial resolution and noise.

Another approach to reduce the effective number of LoRs and to accelerate image reconstruction is to

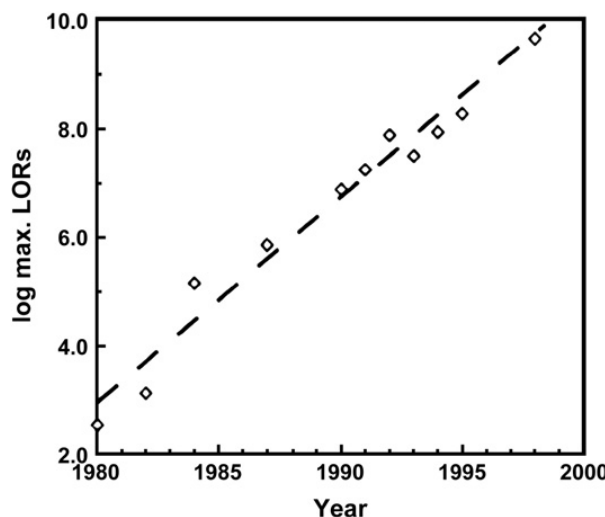


Fig. 7. Increase in the number of lines of response (LoRs) in PET systems (log scale) versus time. (From Brasse D, Kinahan PE, Clackdoyle R, et al. Fast fully 3-D image reconstruction in PET using planograms. IEEE Trans Med Imaging 2004;23:413; with permission. Copyright © 2004 IEEE.)

rebin the 3D data into a stack of 2D slices that can be reconstructed independently using a 2D reconstruction method such as filtered backprojection or a 2D ordered subsets expectation maximization (OSEM) algorithm. Fourier rebinning (FORE) combined with 2D OSEM [75,76] is more than an order of magnitude faster than fully 3D OSEM. Furthermore, it produces images that are not significantly degraded compared with 3D OSEM for whole-body clinical scanners [77]. For high-resolution PET systems, however, the number of counts recorded per LoR is extremely low. As a consequence, the data measured do not reflect accurately the ideal line-integral of the radionuclide activity on which the FORE algorithm relies. Thus, the potential for resolution recovery is lost with this approach [70].

The list-mode processing approach is used widely [78–86]. Using list-mode (or histogram) processing, the computation time is independent of the number of LoRs in the system and instead is directly proportional to the number of counts in the data set. Because the sensitivity of PET systems continues to increase, the computation time for these processing approaches also will continue to increase.

Spatially varying system response model for fully three-dimensional PET

One aim of high-resolution PET is to resolve and quantify very low concentrations of PET molecular probes distributed in small target volumes. Realizing the potential spatial resolution and contrast performance of high-resolution scanners requires incorporating an accurate model of the system blurring in the OSEM algorithm and performing resolution recovery by iterative deconvolution [70]. The system response matrix (SRM) maps the contribution from each image voxel to each detector pair and conveniently represents the imaging process. Storing the SRM in memory is a challenging problem for model-based PET image reconstruction. The size of the SRM is proportional to the number of LoRs in the system, and even though it is highly sparse, the SRM can be gigantic. This issue has been addressed by several approaches that combine special hardware implementation and data representation [87]. Some implementations of the SRM assume the perfect line-integral model and neglect image-degrading effects such as intercrystal photon scatter, photon acollinearity, positron range, and crystal penetration [88,89]. This approach allows one to compute the SRM on the fly. Other implementations of the system matrix try to incorporate accurate physical models to deconvolve resolution-blurring effects effectively and recover spatial resolution [70,90]. The SRM can be factored into different components; some of them are precomputed, whereas others are recomputed for each scan to save memory [91].

Some components can be modeled by convolution kernels in the sinogram space and others by processing in the image space [70,92]. Full system modeling often is performed through extensive Monte Carlo simulation [93] or analytic modeling [94].

Other researchers have studied the benefits and computational challenges of including spatially varying models in fully 3D PET reconstruction. Panin and colleagues [95,96] investigated fully 3D PET image reconstruction with a spatially variant system matrix. Their implementation required 360 MB of memory to store the point spread function components for the Hi-Rez scanner (Siemens Medical Solutions, Knoxville, Tennessee) ($168 \times 168 \times 313$ projection data bins) with an image voxel size of $4 \times 4 \times 2 \text{ mm}^3$. Each iteration required a 1-minute run-time on nine dual central processing unit (CPU) nodes (18 CPU cores). For their study, they performed 60 OSEM iterations with 21 subsets (16 angles per subset). Herraiz and colleagues [91] also investigated fully 3D PET image reconstruction using 28.8×10^6 fully 3D LoR histograms for the GE/Suinsa eXplore Vista DR system. Images were reconstructed on a $175 \times 175 \times 62$ voxel grid ($0.38 \times 0.38 \times 0.78 \text{ mm}^3$). For an Advanced Micro Devices (Sunnyvale, California) Opteron 244 1.8 GHz cluster with nine dual-CPU nodes, each iteration with 50 subset updates requires 5 minutes. Exploiting symmetries, up to 150 MB of memory was required to store the SRM.

In summary, iterative, fully 3D image reconstruction algorithms that incorporate spatially varying models can improve the quality and quantitative accuracy of image reconstruction for PET at a substantially higher computational and memory cost. Further, as the number of LoRs and system sensitivity increase (enabling higher reconstructed resolution but a greater number of image voxels), the cost of applying accurate system models and scatter correction further increases, preventing a wider use of these techniques to improve image quality and quantification. To address the limitations of small-animal PET arising from computational complexity, a cost-effective (ie, not a CPU cluster) technology advance is needed that enables substantial acceleration of reconstruction using strategies that include an accurate spatially variant system model, regardless of collected data format.

Contrast and contrast resolution

The ability to differentiate and quantify one focal region of probe accumulation from the background (contrast) or two adjacent regions of focal probe accumulation with slightly different concentrations (contrast resolution) depends strongly on the level of background present. This background has two main components. First, there typically is nonspecific targeting of the probe in cells surrounding

the ROI. The extent of this effect depends on the molecular probe design, the physiology of the subject, and the biology of the target [97]. Second, processes such as photon scatter in the tissue, random coincidences, the partial volume effect, pulse pileup, and line forward projection and backprojection during image reconstruction will place counts outside the desired target volume in the reconstructed image and into the surrounding background, degrading contrast and accuracy. The impact these factors have on background depends on certain performance parameters of the system. The partial volume effect [98] on contrast recovery is mitigated by designing the system to achieve high spatial resolution [99].

Effects of photon scatter in tissue

In PET each photon detector signal from every pair coincidence event is processed individually for spatial, energy, and arrival time information. Photons that undergo scatter in the tissue before reaching the detector lose energy, depending on the scatter angle [100]. The amount of energy lost by a photon undergoing Compton scatter interaction versus the scatter angle is determined by the well-known formula determined by considering the kinematics of Compton scatter:

$$E_c = E_i / [1 + (E_i / 511)(1 - \cos\theta)] \quad (3)$$

where E_c and E_i are, respectively, the photon energies after and before the scatter, and θ is the scatter angle relative to the incoming photon direction.

To mitigate event-mispositioning errors from tissue-scattered photons, an electronic lower and upper threshold of pulse height (ie, the energy window setting) is imposed on each incoming detector signal. The effects of tissue photon scatter on the background level can be reduced by implementing a very narrow energy window [101]. If the window setting is narrower than roughly a factor of twice the natural energy resolution of the system, measured at FWHM of the typical Gaussian-shaped photopeak in a measured pulse height spectrum, photon sensitivity will be compromised. On the other hand, if a relatively wide energy window around the 511-keV peak energy is selected (eg, 350–650 keV), the image data set will include a significant fraction of events in which one or more photons have scattered in the tissue. A detector system with excellent energy resolution allows the use of a narrow energy window setting to reject contamination from tissue-scattered photons while preserving high photon counts from the photopeak. The typical energy resolution capability for available small-animal PET systems is on the order of 19% to 75% FWHM at 511 keV

[40–42,45,46,65,66,102]. With a standard 59% window setting at 511 keV (350–650 keV), it can be seen from Equation 3 that photons that scatter 68° or less are accepted into the image data and, depending on the size and activity of the animal, there could be significant contamination by tissue scatter (as well as by random coincidences), thus limiting contrast resolution and quantitative accuracy.

Positioning errors from photon Compton scatter in crystals

In addition to the problem of penetration, annihilation photons often undergo Compton scatter in the crystals, causing them to leave a small crystal element and the line of entrance and enter into adjacent crystals. For high-resolution (small-crystal) systems, crystal scatter causes energy to be deposited in more than one crystal, which can be a source of substantial positioning errors and thus contrast loss in high-resolution PET systems. This crystal scatter is more likely to occur with lower-Z, lower-density crystals, such as GSO, than with higher-Z, higher-density crystals such as BGO. Fig. 5 shows the distribution of 511-keV photon interactions for a photon entering obliquely into an LSO array of $1 \times 1 \times 10 \text{ mm}^3$ pixels. The Compton scatter interactions are the energy depositions seen off the line of entrance. Mispositioned crystal scatter events contribute to the tails of the response function (but not the FWHM) and represent approximately 25% of the detected events. The probability of crystal scatter is higher for relatively low-Z, lower-density crystals such as GSO and cadmium zinc telluride (CZT), where on average each incoming 511-keV photon produces approximately two interactions in the crystal (a scatter followed by a photoabsorption) but occurs significantly in higher-Z crystals such as LSO as well (see Table 1) when the crystal elements are small. In high-resolution PET systems crystal scatter out of small crystal elements can be a major source of event-positioning error, which in turn can degrade contrast and contrast resolution. Crystal scatter is not as much a problem in standard clinical systems with larger crystal elements ($\geq 4 \text{ mm}$ width), because a larger crystal is more likely to completely absorb the energy from two or more interactions.

The currently available position-sensitive PET scintillation detector, whether for clinical or preclinical scanners, uses light multiplexing in the scintillation crystal array [103] and/or charge multiplexing in the position-sensitive photodetector [104] or associated readout circuit [105], resulting in a few (typically four) readout channels. Such detectors have only 2D positioning capabilities. That is, they estimate the 2D photon interaction coordinates (x-y) for each event by determining

the array crystal closest to the 2D weighted mean of the readout signals. Thus, the standard PET scintillation crystal detector designs in available small-animal PET systems [40–42,45, 46,65,66,102] cannot determine whether intercrystal scatter occurs within a detector module, because only an energy-weighted mean position is determined for each incoming photon event. Intermodule scatter events in standard detectors typically are rejected because the 511-keV energy window setting is applied to each module independently, thus reducing photon sensitivity. Because individual interaction coordinates and the corresponding energies deposited in multi-interaction photon events cannot be determined in the standard PET detector, the result is substantial positioning errors that translate to loss in contrast recovery.

Effects of random coincidences

As is the case for scatter coincidences, random coincidences can be a significant source of background counts and contribute to degraded contrast and less accurate quantification. For a PET system with random coincidence background rates, R_{ij} , measured along any given LoR between any two crystal elements i and j with recorded single-photon rates S_i and S_j , respectively, the rate of this background source may be estimated by the equation $R_{ij} = 2\Delta t S_i S_j$, where Δt is the coincidence time window setting. Thus, to reduce the effects of background, the time window should be as narrow as possible, and the single-photon rates recorded throughout the system should be as low as possible. Analogous to the case for the energy window, if the coincidence time resolution is excellent, the coincidence time window setting can be narrow (but approximately twice the coincidence time resolution) without degrading photon sensitivity. The typical coincidence time resolution of commercially available systems is on the order of 2 ns FWHM [40–42,45,46,65,66,102]. The random coincidences rate along each LoR also can be estimated via measurement using the delayed coincidence window method [106] and subtracted on-line. A common figure of merit for SNR in PET in the presence of background events from tissue scatter and random coincidences is the noise equivalent count (NEC) rate [107], which, when using a method that analytically estimates random coincidences ("randoms"), is defined as the ratio of the true coincidence ("trues") rate to the square root of the totals (trues + scatter + randoms) rate.

Is time-of-flight PET useful for small-animal PET?

Recently there has been renewed interest in the concept of time of flight (ToF)-PET because of the

development of high-Z, high-density scintillation crystal systems that also achieve superior coincidence time resolution (≤ 1 ns FWHM) [108]. This excellent coincidence time resolution makes it possible to constrain each event and subsequent line projections performed during image reconstruction to a smaller region along each LoR. This constraint improves the SNR via the signal-to-background ratio in the image reconstruction process [109,110]. The FWHM of the constrained line projection is $\Delta l = c \times T_r / 2$ [111], where c is the speed of light and T_r is the FWHM coincidence time resolution. For example, if $T_r = 500$ ps FWHM, then the line projection is spread in a Gaussian distribution with FWHM = 7.5 cm centered on the estimated emission point. Such a ToF resolution does not itself provide adequate spatial resolution to avoid the need for the forward and backward line projection reconstruction methods, but the constraint does facilitate improvements in SNR because essentially more counts are placed in a smaller region along an LoR, which also can enhance contrast. The contrast improvement from ToF along any LoR is roughly equal to the square root of the ratio of the subject thickness along that line to the FWHM of the constrained line projection [111]. Thus, there is potential for significant improvement in SNR for imaging the trunk of the human body, perhaps by a factor of two to five, depending on subject size. For small-animal or dedicated organ imaging such as breast imaging, however, there is no improvement in SNR with the coincidence time resolution of current ToF-PET detector technologies because the size of the object under study is on the order of the size of the ToF line constraint (eg, < 8 cm).

Promising future technologies for small-animal PET

This section presents what authors believe are promising new high-resolution PET technologies that are under development at various research centers around the world to address the presented challenges in advancing small-animal PET. These technologies have not yet been implemented into full systems. One advantage that small-animal PET has over its clinical counterpart is that, because the system is much smaller in size, promising new and exotic materials and methods may be investigated at a reasonable cost.

New strategies to increase the photon sensitivity

Geometrical arrangement of detectors

If one considers a point source placed at the center of the system with fixed transaxial and axial FoV

widths (Fig. 8A), arranging rectangular detectors into a four-sided polygon (ie, a square or rectangle) provides the highest sensitivity of all possible detector geometries [61]. Many photons undergo crystal scatter, and in general the four-sided system polygon has smaller gaps through which these photons can escape [61]. This fact is true for both small-animal and clinical system geometries, although for the latter the differences in photon sensitivity between a cylindrical and rectangular geometry are reduced because the system diameter, detector modules, and individual crystal elements are larger, and the inter-module gaps are smaller; therefore a lower fraction of scatter photons escape. If the corner gaps of the box-shaped system built from semiconductor CZT detectors are filled (see Fig. 8B), a significant additional boost in photon sensitivity is possible, resulting in approximately 19% center point source photon sensitivity for a very narrow 496- to 526-keV energy window [61]. Another advantage of the four-sided system is that it is relatively easy to design the system to allow movable heads with selectable FoVs to bring the detectors closer to the subject and accommodate subjects of different sizes, thus enabling a second additional boost in photon sensitivity by increasing geometric efficiency. Using detectors capable of measuring

photon DOI [41,112–118], one can bring the detectors closer together for increased photon sensitivity, and hence enhanced image SNR, while mitigating parallax errors that blur spatial resolution (see Fig. 6). Another complementary method to improve the geometric efficiency, aside from moving the detectors closer to the subject contours, is to incorporate as large an axial span of detectors as possible, which is the approach used in certain new commercially available designs [47,50].

Potential solution to the problem of reduced light collection efficiency as a function of crystal length (photon sensitivity) for small crystal elements

Photon sensitivity also can be improved by increasing the effective crystal length (ie, the thickness seen by incoming photons), thereby increasing intrinsic detection efficiency. But high-resolution crystal rods, which must be very narrow, have poor light collection as their length increases, and nearly all available designs use relatively short crystals (approximately 10 mm) [40,42–44, 47,49,50,52,53,65,66]. A new scintillation detector configuration under study [68,119–121] incorporates thin photodetectors that read the light from the sides (Fig. 9B) rather than from the ends

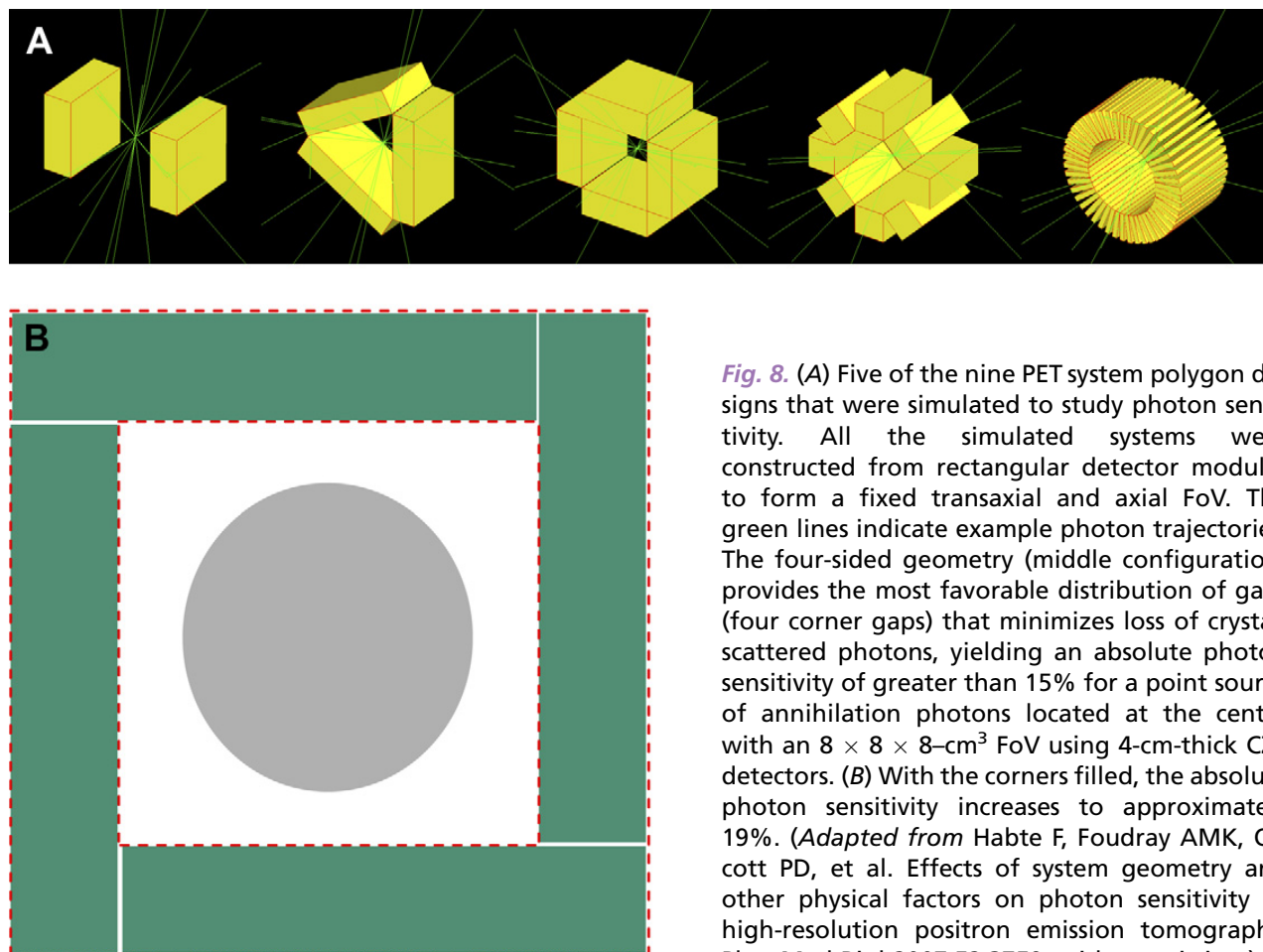


Fig. 8. (A) Five of the nine PET system polygon designs that were simulated to study photon sensitivity. All the simulated systems were constructed from rectangular detector modules to form a fixed transaxial and axial FoV. The green lines indicate example photon trajectories. The four-sided geometry (middle configuration) provides the most favorable distribution of gaps (four corner gaps) that minimizes loss of crystal-scattered photons, yielding an absolute photon sensitivity of greater than 15% for a point source of annihilation photons located at the center with an $8 \times 8 \times 8\text{-cm}^3$ FoV using 4-cm-thick CZT detectors. (B) With the corners filled, the absolute photon sensitivity increases to approximately 19%. (Adapted from Habte F, Foudray AMK, Ollcott PD, et al. Effects of system geometry and other physical factors on photon sensitivity of high-resolution positron emission tomography. *Phys Med Biol* 2007;52:3759; with permission.)

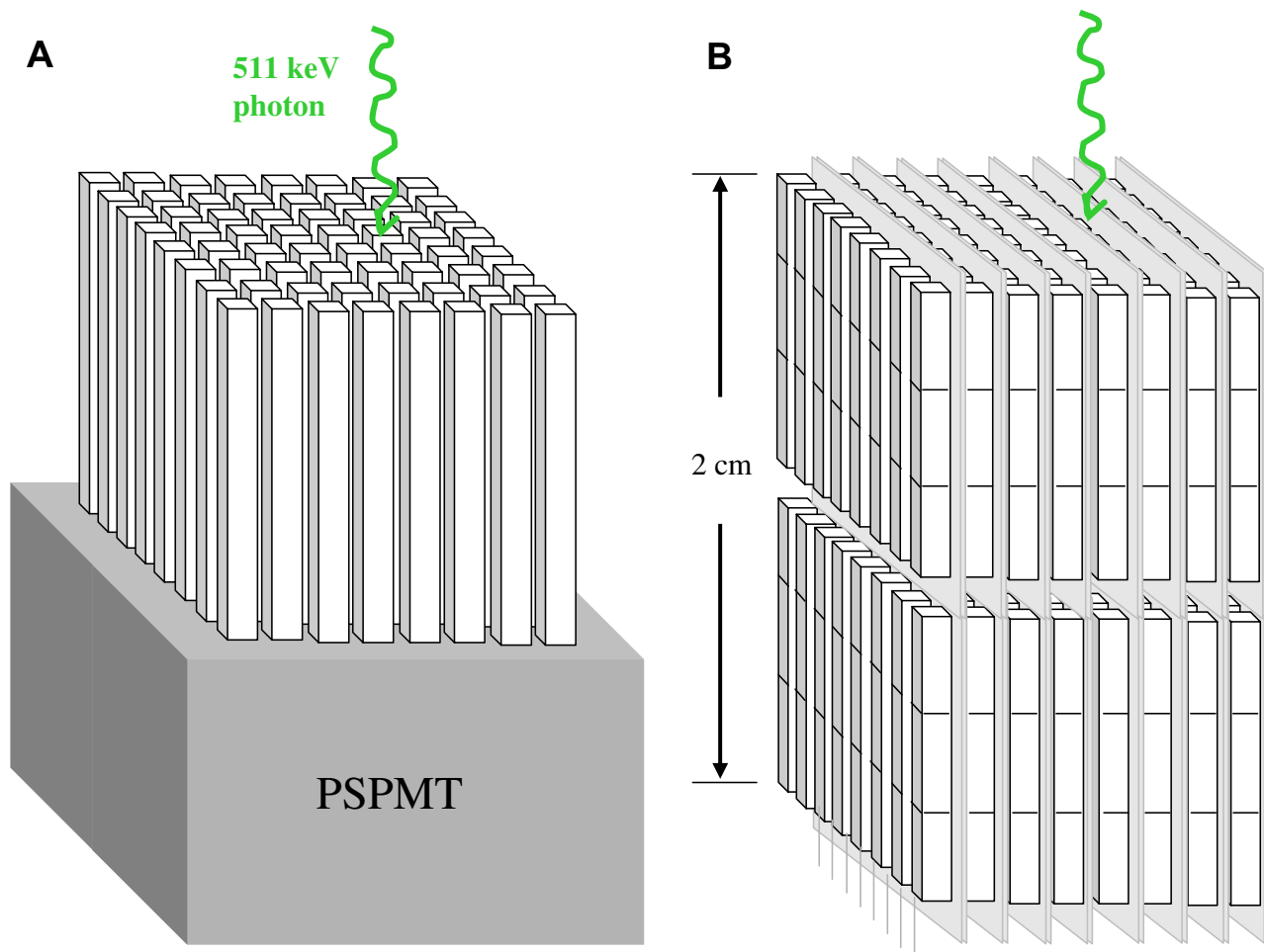


Fig. 9. Instead of the conventional scintillation array readout geometry (A), the enhanced scintillation light collection configuration (B) is achieved in an imaging array configuration using very thin semiconductor photodetectors placed in between crystal array layers. In the design shown, each scintillation detector layer comprises two crystal arrays coupled to two independent photodetectors. Each scintillation detector layer operates independently. In this arrangement, incoming photons encounter a minimum crystal thickness of 2 cm. Because the semiconductor photodetectors can be position sensitive, the latter design also facilitates a direct measurement of the 511-keV photon interaction depth to mitigate radial resolution blurring artifacts.

of each crystal (Fig. 9A). Because of its high scintillation light collection aspect ratio, this configuration yields the same high light collection efficiency ($> 90\%$) independent of crystal length [68]. Thus, long crystals can be used to preserve high photon sensitivity while achieving high performance in other parameters that depend critically on the light signal (eg, energy, time, and spatial resolutions). In this new design, a very thin photodetector is placed between crystal planes. The photodetector must be thin to preserve a good crystal packing fraction (the fraction of area seen by incoming photons that is covered by crystal). Extra-thin position-sensitive avalanche photodiode (PSAPD) photodetectors have been manufactured for these purposes (Fig. 10A) [120,121]. Further increases in packing fraction are accomplished using recently developed very thin (approximately 65-micron) polymer-based specular reflector material between crystals.

Compared with scintillation materials such as LSO and BGO, semiconductor CZT detectors have relatively low Z and low density (as in the GSO scintillator), and it is challenging to manufacture good-quality detectors thicker than 5 mm. Thus, to achieve high detection efficiency, the 5-mm thick detector slabs are arranged edge-on with respect to the general direction of incoming annihilation photons so that the photons traverse CZT material with a minimum thickness of 4 cm [61,122,123]. Because no intercrystal reflector is required in this CZT design, the crystal packing fraction is potentially much higher ($> 99\%$) than for pixellated scintillation crystal designs, so fewer photons escape through gaps between crystals [61]. When a non-scintillating semiconductor crystal (eg, CZT) PET detector technology is used (Fig. 10B) [61,122,123], light collection is not an issue, and the crystals can be configured with a greater than 99% intermodule packing fraction.

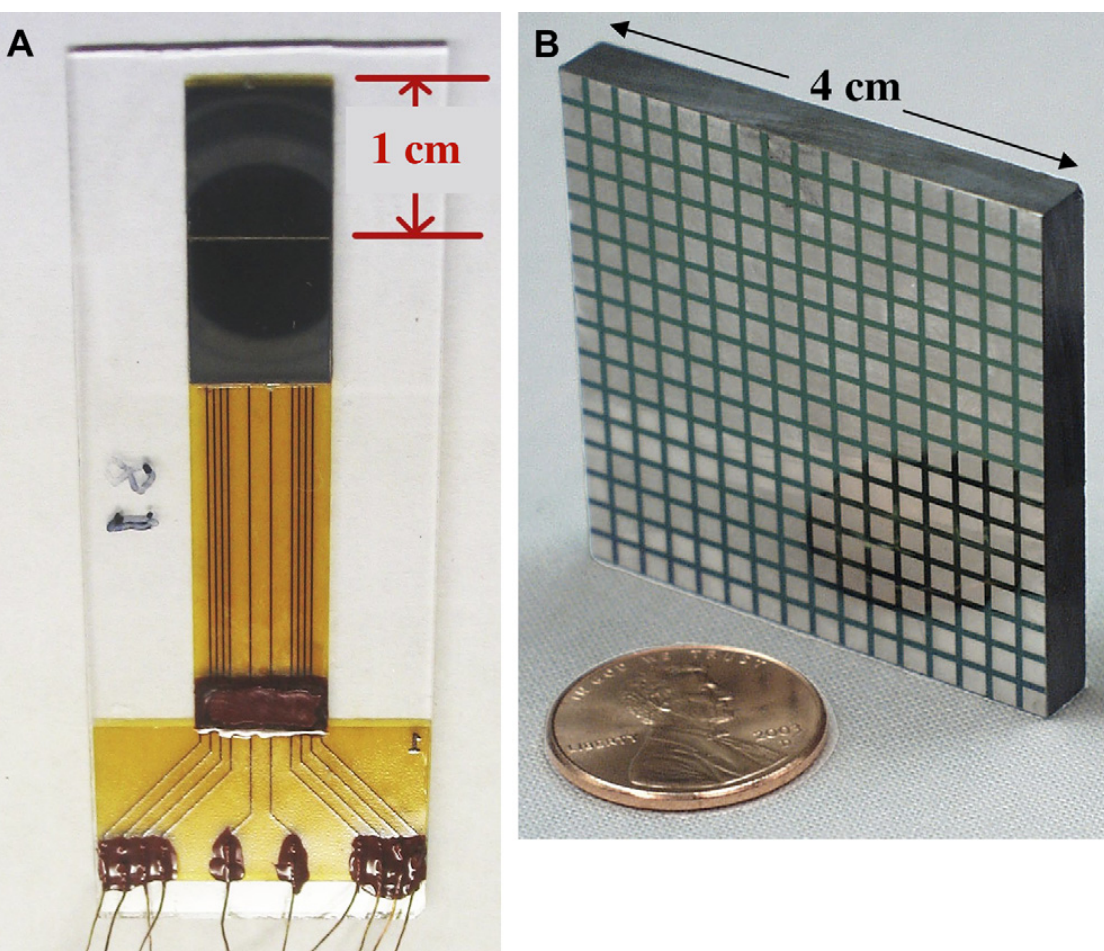


Fig. 10. Two semiconductor detector designs that facilitate 3D positioning of the 511-keV photon interaction coordinates. (A) The extra-thin dual-PSAPD photodetector module. The thin device comprises two PSAPD chips approximately 200 μm thick mounted on a single flex circuit that is 50 μm thick. The flex circuit delivers bias to each PSAPD and enables readout of the four corner signals for positioning. With an LSO array mounted to each chip, and each scintillation detector layer oriented edge-on, incoming photons encounter a minimum scintillator (eg, LSO) thickness of approximately 2 cm with directly measured photon interaction depth (see Figure. 9B). (B) A $40 \times 40 \times 5\text{-mm}^3$ CZT array. The 256-pixel device shown has 2.25-mm anode pixels (indium) deposited on a 2.5-mm pitch. The back side has a continuous cathode. Incoming photons encounter a minimum crystal thickness of 4 cm. Direct measurement of their interaction depth is possible via the signals induced on the pixels.

The new scintillation [68,119–121] and semiconductor [122,123] detectors under study for small-animal PET can position the 3D coordinates of photon interactions, enabling the use of relatively long (thick) crystals for high intrinsic efficiency in detection while mitigating other photon-penetration and scatter effects associated with thick crystals.

Novel algorithmic approaches to recover single and tissue-scattered photons

Using detectors capable of estimating the 3D coordinates of the individual interactions has the benefits of (1) eliminating parallax positioning errors to facilitate uniform spatial resolution throughout the system FoV and (2) providing a more accurate estimation of the first interaction for improved photon positioning and thus reconstructed spatial resolution. These 3D-positioning capabilities also have other benefits. Resolving individual photon interactions in the detector actually provides an

opportunity to include background single and tissue-scattered photon events that normally are rejected from the PET data set, thus effectively increasing photon sensitivity [124,125]. By using more sophisticated image-reconstruction algorithms that incorporate the knowledge of the energy and location of individual interactions in the detector and the physics of Compton scatter, it may be possible to include (1) unpaired single photons [124] (normally rejected by the coincidence criteria) and (2) tissue-scattered coincidence photons [125] (normally reduced by photon energy discrimination) into the data set without loss of spatial resolution or contrast.

Depending on the system photon sensitivity, the number of single unpaired annihilation photons detected by the system can be an order of magnitude or more higher than the number of paired coincident photons (as is the case for standard clinical systems, because they typically have a relatively low

ratio of detector axial FoV to diameter). Also, the number of tissue-scattered coincident photons can be substantial, especially for clinical imaging, but even for rats [101]. Using a 250-keV energy threshold, tissue-scatter events can be >70% of all coincident photon events for PET imaging of the human thorax [126]. Thus, a method of including these normally rejected photons into the image reconstruction process without compromising spatial resolution and contrast [124,125] could, in effect, increase the photon sensitivity by an order of magnitude or more, greatly enhancing photon-counting statistics and thus SNR. To enable high-resolution reconstructions for the recovered single-photon data, the reconstructed coincidence photon image data were used as a prior. Preliminary data [125] show that by effectively increasing the counts in the reconstructed data set, the SNR (mean/variance) is improved substantially without compromising spatial resolution or contrast [124].

New strategies to enable increased spatial resolution

Approaches to avoid complex and expensive assembly of high-resolution detectors

One approach under investigation to address the bottleneck of higher-resolution systems requiring more complex scintillation crystal arrays is the use of semiconductor crystals such as CZT (see Fig. 10B) [61,122,123], instead of scintillation crystals (see Table 1). To achieve high photon sensitivity, the semiconductor crystal arrays are arranged edge-on with respect to incoming photons. A similar design was implemented recently in a small-animal PET system using smaller cadmium telluride detectors [127]. In semiconductor crystals, a strong electric field is established across the crystal by applying a relatively large potential difference on the two electrodes (anode and cathode) on either face of a monolithic crystal slab, as depicted in Fig. 10B. An incoming annihilation photon interacts with the atoms in the semiconductor crystal and creates electron–hole pairs, just as it would in an inorganic scintillation crystal. In the presence of the electric field, however, the electron–hole pairs are separated, drift toward opposite faces (electrons toward the anode, holes toward the cathode), and are detected directly. The motion of the charge induces signals on the respective electrodes that may be used to extract spatial, energy, and temporal information. Thus, semiconductor detectors directly sense the ionization signal created by the annihilation photon absorption and do not create, transport, and collect scintillation light [128,129].

In semiconductor detectors, fine spatial pixellation is set by the segmented pattern of charge-collecting electrodes deposited on the crystal slab

faces, rather than relying on cutting, treating, and assembling many minuscule crystal pixels. In the most common design, the anode plane is segmented into tiny square conductors (see Fig. 10B), the cathode is a continuous plane, and the x-y interaction coordinate is determined by the pattern of charge induced on the anode plane [130]. A less common design is to use a set of parallel, very thin linear strips across the anode and an orthogonal set on the cathode [131]. In this case the x-y coordinate of the interaction is determined by the intersection of the strips on either side of the crystal slab that record a signal above threshold. In either case, to achieve high intrinsic spatial resolution, one deposits the electrodes with a pitch that matches the desired spatial resolution (eg, 0.5 mm). The advantage of the cross-strip electrode design is that fewer electronic channels ($2n$ versus n^2 , where n is the number of readout electrodes) are required to achieve a given intrinsic spatial resolution than in the square pixel design.

Increasing the light signal available from small scintillation crystals

One approach under investigation [68,119–121] to increase light collection efficiency for high-resolution scintillation crystal designs is to read out the larger side faces of the long and narrow crystals (see Fig. 9B) rather than the small ends of the crystals (see Fig. 9A), thereby substantially improving the light collection aspect ratio [68]. In this new geometry, (see Fig. 9B) with the photodetector plane generally edge-on with respect to incoming annihilation photons, the scintillation light collection is nearly complete (> 95%), independent of individual crystal length, width, and surface treatment, as well as origin of the scintillation light [68]. These factors help achieve high energy and temporal resolution, in addition to high spatial resolution, simultaneously. To accomplish this feat in an array, while maintaining high crystal packing fraction, very thin semiconductor photodetectors are configured between the crystal planes (see Fig. 9B). If the thin photodetector is position sensitive, the annihilation photon interaction depth may be measured directly as well [68,119–121]. Extra-thin PSAPD photodetectors have been manufactured for these purposes (see Fig. 10A) [120,121]. Because in this new crystal-photodetector configuration the light signal is the same, independent of crystal surface treatment, fine-ground “as cut” surfaces can be used to reduce crystal processing costs substantially.

Of course another design strategy that avoids the problem of lower light signals from small scintillation crystal elements altogether is not to use them at all. The direct-detector approach [61,122,123], in

which semiconductors directly sense the charge in the form of electron-hole pairs created from absorption of an annihilation photon (see Fig. 10B), completely avoids the pitfalls associated with creation, propagation, and collection of scintillation light in minuscule scintillation crystals.

Reducing the effects of photon penetration and parallax positioning error

Measuring annihilation photon interaction depth may be accomplished with 3D-positioning detectors, that is, detectors that are capable of localizing the 3D interaction coordinates of the incoming photon. The standard PET block-detector designs used in small-animal PET [40–46] determine the 2D coordinates of the energy-weighted mean of interaction locations but cannot localize or identify the individual interactions separately. A few small-animal PET detector designs have been built that enable the location of the third dimension of the weighted mean photon interaction to be determined [41,115,117,118], but because they multiplex many crystal array elements into four readout channels, these designs do not localize the individual interactions separately. In the new scintillation detector design with edge-on PSAPDs configured on the sides of minuscule LSO scintillation crystal elements [68,119–121], 3D-positioning capability may be attained by segmenting the crystal fingers into arrays (see Fig. 9B). For nearly all incoming photon events, this design allows the 3D interaction coordinate(s) (x , y , z) of individual interactions to be measured directly. That is, with this new detector design the individual photon interactions are each localized in 3D space, rather than just their energy-weighted mean as provided by most other scintillation detectors.

In the cross-strip CZT design, the detectors are also arranged edge-on and provide the 3D coordinates of individual interactions. As stated, in the planes parallel to the electrodes, the x - y interaction coordinate for an event recorded in any given slab is determined by the intersection of the signals recorded in the orthogonal strips. The third coordinate along the direction orthogonal to the cathode and anode plane may be determined using the ratio of the cathode-to-anode signal pulse heights [122,123,131]. Point-spread function measurements with the cross-strip detectors indicate that the resolution along the edge (parallel to the electrodes) is defined precisely by the pitch of the anode or cathode strip [122,123,130,131], depending the direction in which the beam is translated. In the cathode-to-anode direction (orthogonal to the electrodes), the intrinsic resolution is below 1 mm FWHM [122].

To study the effect on image quality of resolving the photon interaction depth in a 3D-positioning

detector, the authors simulated an $8 \times 8 \times 8$ -cm³ FoV box-shaped PET system built from the high-resolution $40 \times 40 \times 5$ -mm³ cross-strip CZT detectors and acquired a simulated PET acquisition of a high-resolution sphere phantom as a function of the detector resolution along the photon interaction depth direction. (The resolution of the other two coordinates was assumed to be 1 mm.) Fig. 11 shows the resulting reconstructed images. Because of the interaction depth-resolution capability, the spatial resolution is essentially uniform all the way out the edge of the system FoV (the detector aperture equals the useful FoV) but is noticeably more uniform near the edges of the FoV for the 3-mm (Fig. 11A) than with the 5-mm (Fig. 11B) depth-resolution capability.

Potential solutions to address image reconstruction complexity for high resolution PET

The use of 3D-positioning detectors further increases the computational challenges of high-resolution PET image reconstruction as described earlier. 3D-positioning detectors provide additional photon-depth positioning bins for each crystal element entered, giving the capability of photon interaction depth resolution, which mitigates parallax positioning errors and facilitates uniform spatial resolution. The third positioning coordinate also potentially enables a higher degree of spatial sampling to help recover signals that have high spatial frequency, provided that additional sampling is indeed required per the Nyquist-Shannon sampling theorem [132]. Using 3D-positioning detectors, however, increases the number of system LoRs or, alternately, the number of non-zero elements in the system response matrix by orders of magnitude. For example, PET systems with 3D-positioning detectors with resolutions of 1 mm or less are under construction [72,124,133] that contain up to 8 billion LoRs, and other such billion-LoR PET systems have been built [134]. With the increased photon sensitivity and better SNR proposed by these and other systems, resolution-recovery techniques can be used to reconstruct higher-resolution images. As a result, the number of image voxels has grown at a rate similar to the increase in the number of LoRs.

It is clear that robust, statistical-based image reconstruction algorithms, such as 3D OSEM, ideally with spatially variant response models, are needed to process this mass of data and recover the desired system spatial resolution with an acceptable SNR [64]. It also is clear that fast and memory-efficient line forward and backprojection operations are needed to process these enormous data sets and incorporate spatially varying

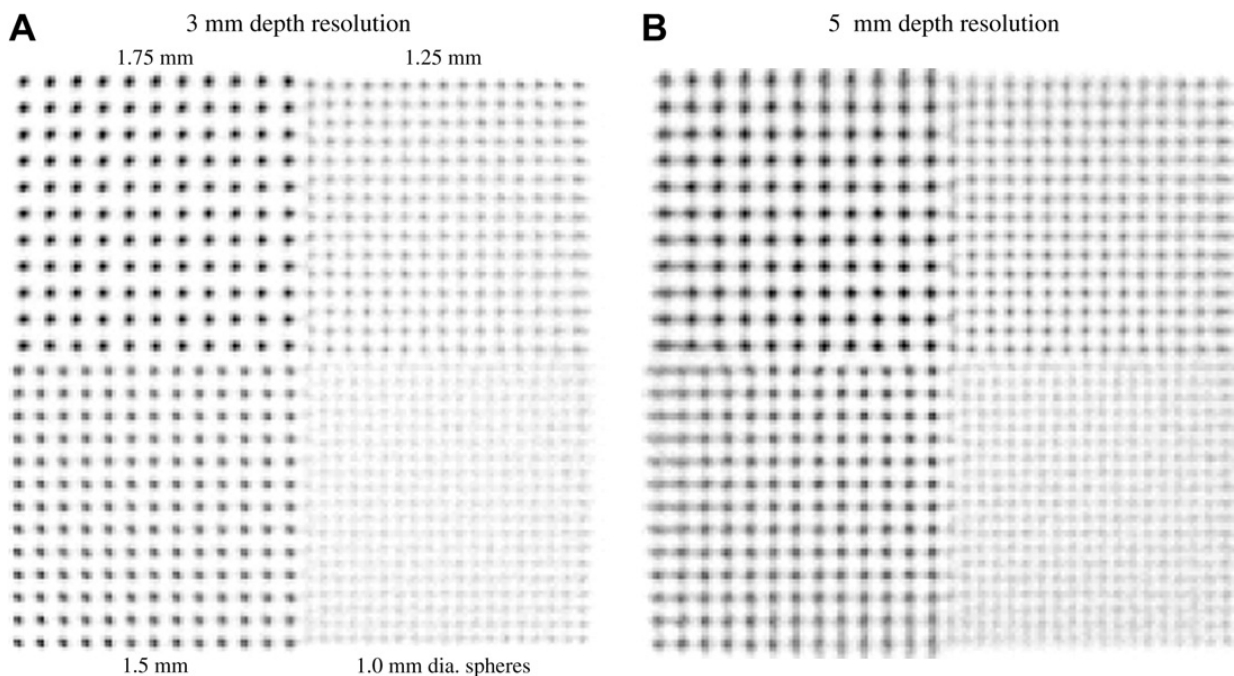


Fig. 11. Reconstructed sphere resolution phantom (1-, 1.25-, 1.5-, and 1.75 mm diameter with pitch equal to twice the diameter) acquired in a Monte Carlo-simulated PET system ($8 \times 8 \times 8\text{-cm}^3$ FoV) built with a cross-strip CZT detector design [122,123], for two different photon interaction depth resolutions: (A) 3-mm and (B) 5-mm cathode strip pitch. To simulate realistic detector resolution, each interaction of each incoming photon event was binned to the center of the nearest $1 \times 1 \times \Delta d\text{-mm}$ detector voxel defined by the strip electrode pattern, where Δd is the photon interaction depth resolution (see Fig. 6). Images were reconstructed with 20 iterations of list-mode 3D OSEM [136]. Note that unlike most resolution phantoms, this one extends all the way out to the edge of the $8 \times 8\text{-cm}$ transaxial FoV of the system defined by the detectors (see Fig. 8). For both depth resolutions, the spheres are well resolved all the way out to the FoV edge (better with 3-mm depth resolution), so that the useful FoV equals the detector FoV.

detector-response models and scatter-correction techniques [86]. Finally, processing algorithms whose complexity does not depend on the number of LoRs also are required to process efficiently the extremely sparse data generated by high-resolution PET systems with minimal memory storage requirements. Using list-mode processing [78–86], the computation time is independent of the number of LoRs in the system and instead is directly proportional to the number of counts in the data set. Because the photon sensitivity of PET systems continues to increase with ongoing advances, the system records more events for a given imaging study, and thus the computation time for list-mode processing also will continue to increase.

To explore ways to incorporate a resolution-blurring model, it will be more practical to implement it in list mode or histogram mode as opposed to sinogram mode. A sinogram bin is made of the contribution of many LoRs. The symmetries that were present in these LoRs might disappear in the resulting sinogram. The rotational invariance usually is preserved by sinogram binning, but the translational invariance is lost because sinogram storage assumes constant spacing of the projection lines. Maintaining translational invariance is quite important for some systems.

For example, box-shaped PET systems under development [124,133] have more translational invariance than rotational invariance. Exploiting all symmetries is very desirable because it greatly simplifies the task of modeling the blurring for each individual LoR. When images are reconstructed from data stored in list-mode format, it is possible to make use of all available symmetries of the system to accurately model the inherent system resolution blurring, because all data (eg, 3D coordinates, arrival time, energy, and so forth) for every possible LoR are preserved. In addition, list mode facilitates the on-the-fly creation of resolution-blurring models because each list-mode element is a detector pair; in contrast, a sinogram bin can represent, for example, 200 LoRs, and thus needs a more complex model to represent the system accurately.

Most practical image-reconstruction problems do not enjoy a great amount of symmetry, but one is encouraged to make use of any available symmetry. The saving in computing time is well worth the extra care and coding. A polar image representation that allows one to preserve both in-plane and axial symmetries between the LoRs during the system matrix computation was proposed recently to address these issues. This proposal gives rise to

a system matrix having a block-circulant structure [135]. By storing only the nonredundant part of the block-circulant system matrix, memory requirements can be reduced by a factor equivalent to the total number of system symmetries.

New cost-effective, flexible, and powerful image-reconstruction hardware

Inexpensive, off-the-shelf graphics processing units (GPU), a mainstream technology present on graphics cards, are under study [136] to greatly accelerate (1) the two most elementary operations of iterative tomographic image-reconstruction algorithms, the line backprojection and the line forward projection, and (2) accurate modeling of the physical system response. Previous GPU implementations of forward and backprojection were limited to sinogram-based data sets without system modeling and were performed on the old generation of nonprogrammable GPUs [137,138]. The new generation of fully programmable GPUs is under investigation [136] to support the development and drastically accelerate advanced image reconstruction algorithms that incorporate an accurate system model and scatter correction to facilitate the highest spatial resolution and quantitative accuracy. The use of GPUs is particularly practical for image reconstruction because most workstations already have a high quality graphics processor for rendering volumetric images.

Presently, GPUs are more than an order of magnitude faster than CPUs (Fig. 12): An Intel Pentium IV (Intel Corporation, Santa Clara, California) has a theoretical peak performance of 12 billion floating-point operations per second (12 GFLOPs); the NVIDIA GeForce 7900GTX GPU (NVIDIA Corporation, Santa Clara, California), a 2005 technology, has a peak performance of about 200 GFLOPS, higher by almost a factor of 20. GPUs are

characterized by extremely high processing parallelism, fast clock-rate, high-bandwidth memory access, and built-in optimized geometric functions. These characteristics make them particularly well suited for on-the-fly schemes with low memory profiles and high computational requirements. The highly distributed and parallel architecture has allowed GPU performance to increase at a much faster rate than CPU performance. GPUs roughly follow Moore's law squared (see Fig. 12), and so today's difference in performance between GPUs and CPUs—an order of magnitude for similarly priced CPUs and GPUs—will be even greater in years to come. Finally, GPU-based software will be easily updateable, portable, and maintainable. Because GPUs are designed to handle highly parallel geometric computations, shifting most of the algorithm computations from the CPU to the GPU dramatically accelerates list-mode iterative image reconstruction.

Implementation of 3D OSEM on the GPU is challenging because the graphics programming interface was not designed originally for general-purpose computation. It turns out that the two most computationally expensive operations of list-mode 3D OSEM (line backprojection and line forward projection) can be reformulated as pseudorendering tasks that can be run extremely efficiently on the GPU [136]. The preliminary implementation of the list-mode 3D OSEM algorithm on the GPU is more than 40 times faster than an equivalent implementation on a state-of-the-art CPU [136]. Thus, the GPU provides a hardware solution that is highly efficient in dealing with the increasing complexity of high-resolution PET image reconstruction because its computational power is roughly equivalent to that achieved with a 40-CPU cluster but with a cost equivalent to that of a single CPU.

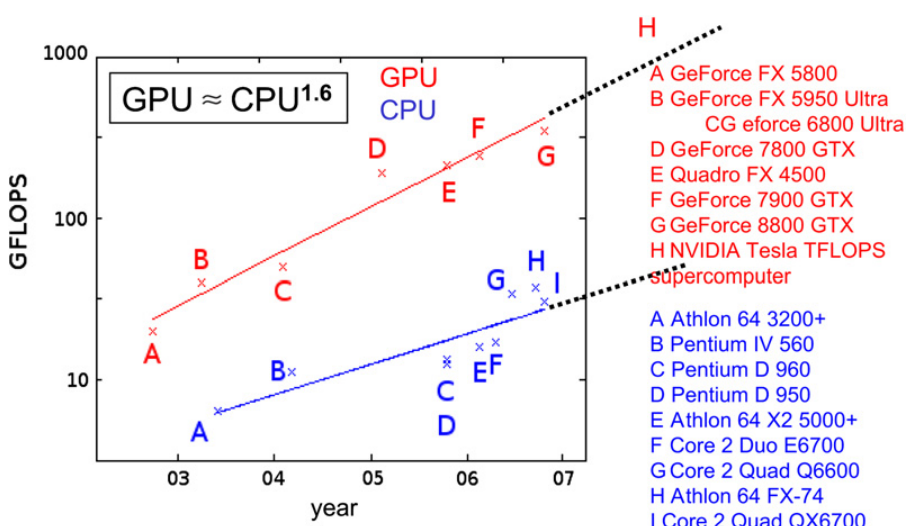


Fig. 12. Comparison of CPU versus GPU raw peak performance slopes. The trend for the increase in GPU performance over time follows a path that is nearly quadratic compared with Moore's law for CPUs. GFLOPS, 1 billion floating point operations per second.

New strategies to enhance contrast and contrast resolution

Reducing the effects of photon scatter in tissue

Consider a PET system design that uses the described LSO PSAPD scintillation detectors with $\leq 12\%$ FWHM energy resolution (see Fig. 10A) [120,121]. With a 450- to 575-keV (24%) energy window centered at 511 keV, this system will have a fraction of accepted events to comparable that of a PET system which has 25% or greater energy resolution [40–42,45,46,65,66,102] and uses a 350- to 650-keV (59%) energy window. With a 450-keV lower energy threshold, however, Compton scatter kinematics (see Equation 3) dictates that only photons that scatter at 30° or less are accepted into the data set. For a system that uses a 350-keV threshold, all photons that scatter 68° or less are accepted into the image data; compared with the 450-keV threshold, there will be significantly higher random and scatter contamination and thus inferior lesion contrast and quantitative accuracy. One advantage of CZT is its superior energy resolution, measured to be less than 3% FWHM at 511 keV [122,123]. Thus, a CZT-based system should require only a very narrow 496- to 526-keV (6%) energy window centered on 511 keV for best photon sensitivity. With a 496-keV lower energy threshold, only the relatively small fraction of photons that scatter at less than 14° would be accepted into the data set, enabling further reduction of photon tissue scatter.

Reducing positioning errors from photon Compton scatter in crystals

High-resolution, 3D position-sensitive detectors can reduce the impact of crystal scatter on positioning errors. Because 3D-positioning detectors are capable of recording the 3D coordinates and energy deposition for every interaction, it is possible to use more intelligent positioning algorithms to better estimate better the line of entrance of an incoming photon and mitigate the effect of positioning errors caused by crystal scattering [139]. Such positioning algorithms may incorporate the physics of Compton scatter and/or a probabilistic formalism such as maximum likelihood to estimate the first interaction location. Fig. 13 shows the results of image reconstruction from a simulated PET acquisition of the sphere resolution phantom in a PET system built from high-resolution 3D-positioning CZT detectors [136,139]. In these data, the coordinates of the first interaction in multi-interaction photon events was estimated using (1) the standard weighted-mean positioning over all interactions and (2) a more intelligent but simple algorithm that estimates the interaction location closest to the weighted-mean position of the second

annihilation photon interacting in the system. As seen in Fig. 13, the latter algorithm, which requires a 3D-positioning detector, greatly reduces the effect of crystal scatter on resolution compared with the weighted-mean approach [139].

Reducing the effects of random coincidences

Because of relatively low activity within the FoV (eg, < 37 MBq) small-animal PET systems typically do not suffer immensely from high random coincidence rates. Besides further improvements in coincidence time resolution, the effects of randoms also can be reduced by applying a narrow energy window to reject single photons that have scattered and that would normally have contributed to the random coincidence rate. Because the random photon coincidence rate increases roughly as the square of the detected single-photon rate, a narrow energy window can be quite helpful in reducing randoms. Fig. 14 shows results of tissue scatter, randoms, trues, totals (trues + scatter + randoms) and NEC rates from simulating a mouse-sized phantom (a cylinder 2.5 cm in diameter and 7 cm in length) in a PET system built from the high-resolution CZT detectors described in the previous section. Because the formation of a signal in a CZT detector relies on the propagation of charge, rather than light, the coincidence time resolution is much worse for CZT than for scintillation detectors. The simulations assumed 8 ns FWHM coincidence time resolution as measured in experiments [122]. Because of the superior energy resolution and very narrow energy window setting (eg, 6% or 496–526 keV), however, a high fraction of the tissue-scattered single (unpaired) photons contributing to the random coincidence rate were rejected. Because the CZT system has high energy resolution, allowing the use of narrow energy window settings without compromising photon sensitivity, the random coincidence rate for the mouse phantom is low, and a relatively high peak NEC is achieved, even though the coincidence time window setting is relatively wide (16 ns) compared with that used for available scintillation crystal systems (approximately 6 ns) [47–52].

Instrumentation and algorithms for combining PET with other imaging modalities

The arguments for combining multimodality data in the context of clinical imaging also hold for pre-clinical imaging where the potential advantages of combining anatomic and functional imaging have been well recognized by biomedical researchers. Multimodality molecular imaging has become an essential tool for the development of new tracers,

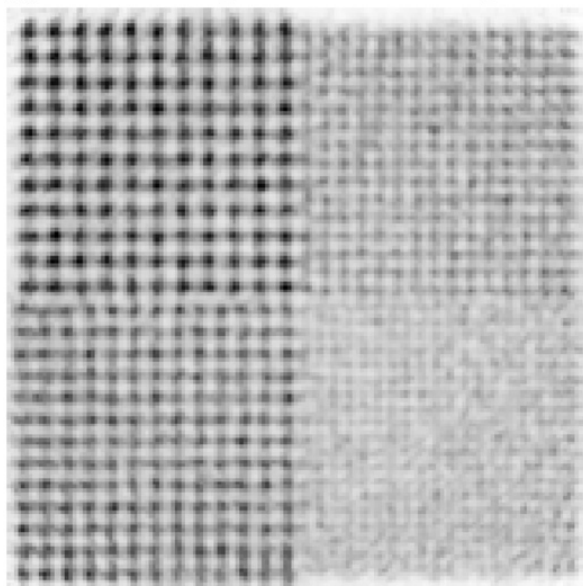
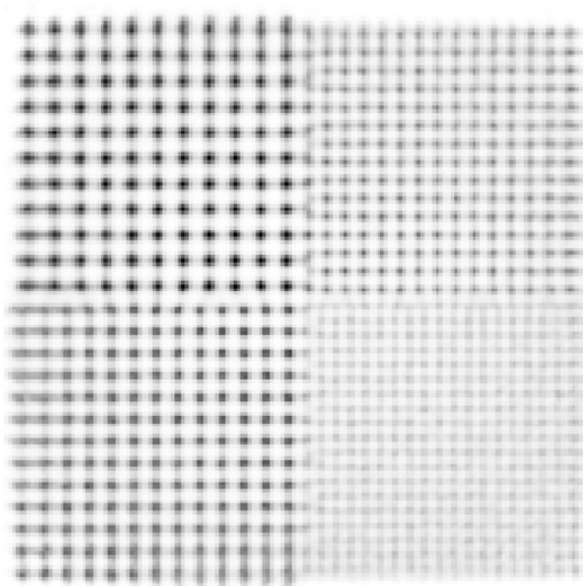
A Positioned at weighted mean of interaction points**B** Positioned at “closest” interaction location

Fig. 13. Reconstructed sphere resolution phantom (1-, 1.25-, 1.5-, and 1.75-mm diameter with pitch equal to twice the diameter) acquired in a Monte Carlo-simulated PET system ($8 \times 8 \times 8\text{-cm}^3$ FoV) using cross-strip CZT detectors [122,123]. Each interaction for every incoming photon event was binned to the center of the nearest $1 \times 1 \times 5\text{-mm}^3$ detector voxel defined by the strip electrode pattern. Images were reconstructed with 20 iterations of list-mode 3D OSEM [136,139]. The data shown used the following multi-interaction photon positioning schemes: (A) Weighted mean over all interaction locations per event; (B) Location of interaction with minimum distance to the other coincident photon position [139].

to study the molecular pathways of disease (including factors such as gene expression) in living subjects, and to test new therapeutic approaches in animal models of human disease. Multimodality imaging, however, requires robust registration of images generated by various modalities. In response to these concerns, several investigators are developing various approaches specifically designed for imaging small animals that allow one to combine the power of PET with other

imaging modalities such as x-ray CT, MR imaging, and optical imaging (OI) [140].

Software-based approaches

A substantial number of techniques have been proposed to achieve the goal of multimodal medical image registration [141,142], but image-registration algorithms widely used in clinical studies have not been well characterized in the small-animal setting. A few investigators focused

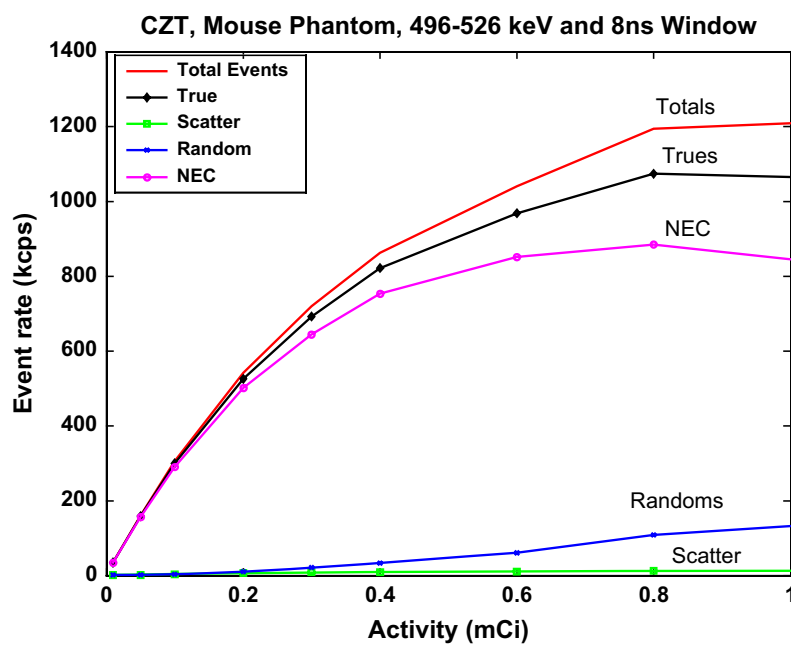


Fig. 14. Coincident rates calculated from Monte Carlo-simulated PET acquisitions in a box-shaped $8 \times 8 \times 8\text{-cm}^3$ FoV CZT system for a mouse phantom (cylinder 2.5 cm in diameter and 7 cm long filled uniformly with ^{18}F activity). The energy resolution and window settings used were 3% FWHM at 511 keV and 6% at 496–526 keV, respectively, and the coincident time resolution and window used were 8 and 16 ns, respectively. Because of exceptional energy resolution, a narrow energy window setting can be used to mitigate both scatter and random background counts while preserving high photopeak counts. Hence, absolute true, total, and NEC rates are relatively high, and random/trues and scatters/trues fractions are relatively low for the proposed CZT system.

on the utility of popular image-registration techniques in various scenarios and using different imaging technologies and reported various degrees of success [143–149]. Some techniques rely on the use of external fiducial markers to aid the registration process, whereas other approaches rely on fully automated algorithms that do not involve user interaction. Current state-of-the-art image-registration techniques allow automatic image registration through a rigid body transformation (eg, using mutual information-based criteria), thus ignoring organ deformation (eg, that caused by respiratory motion). There also has been substantial progress in nonrigid registration algorithms that can compensate for perceived organ deformation for different imaging modalities or can align images from different subjects [150]. Despite the progress made during the last few years, however, many image-registration problems remain unsolved, particularly for small-animal imaging, and image registration is likely to continue to be an active field of research in the future.

Hardware-based approaches

The limitations of the techniques discussed in earlier sections led to the development of hardware approaches that rely on the use of specially designed, custom-made imaging chambers that can be rigidly and reproducibly mounted on separate preclinical scanners (eg, PET and CT). For example, a 3D-grid phantom with 1288 lines was combined with the imaging chamber to derive the spatial transformation matrix from software registration using a 15-parameter perspective model [151]. The average registration error between PET and CT mouse bone scans is less than 0.335 mm. The reproducibility and robustness of the system allows the use of CT images for accurate attenuation correction of the PET data, thus enabling quantitative accuracy [152].

The advantages of the integrated dual-modality imaging systems that are available for clinical applications also are being investigated as a means of facilitating biologic research, especially research involving small animals such as mice and rats [97,153]. Although most commercial dual-modality systems have been configured as single-photon emission computed tomography (SPECT)/CT or PET/CT scanners, several investigators proposed and in some cases have implemented and tested prototype dual-modality systems that combine various imaging technologies such as SPECT and PET [45], PET and OI [154–158], and PET and MR imaging [159–170]. Moreover, efforts to develop trimodality preclinical systems integrated in a single gantry including SPECT/PET/CT [62] and SPECT/PET/OI [171] also are under way.

The YAP-(S)PET scanner described previously allows both PET and SPECT studies to be performed on small animals [45]. Operating the scanner in single-photon mode using the same detector configuration is made possible by mounting a high-resolution parallel-hole collimator in front of each detector module. Likewise, the demand for functional and molecular imaging of small animals using single-photon emitters has stimulated the development of dedicated small-bore high-resolution SPECT systems for imaging mice, rats, small primates, and other mammalian species [172]. Several groups have developed combined SPECT/CT systems designed specifically for small-animal imaging. The most successful designs combine stationary SPECT systems using multi-pinhole collimation techniques [173] with multiple compact detectors having both improved geometric efficiency and a high level of intrinsic spatial resolution including the use of very small scintillator elements read out by position-sensitive or multichannel PMTs or solid-state detectors [174,175]. Trimodality imaging that allows one to combine three modalities and record quasi-simultaneously complementary information gathered from SPECT, PET, and CT might offer many advantages in some situations. One example of such a system is the FLEX Triumph system commercially available from Gamma Medica-Ideas, Inc. [176]. It has been argued that the APD-based detector module proposed by Saoudi and Lecomte [177] is particularly attractive for the design of compact multimodality (PET/SPECT/CT) imaging systems.

Despite the widespread interest in dual-modality imaging, only a few PET/CT prototypes have been developed [44,178–180]. Excellent microCT images of live animals are being obtained using cone-beam x-ray CT imaging and reconstruction [181]. The group at the University of California, Davis (UC Davis) developed a microCT/microPET dual-modality small-animal imaging system for anatomic and molecular imaging of the mouse [178]. The microPET detectors use an LSO scintillator coupled through a fiberoptic taper to a position-sensitive photomultiplier tube. These detectors are placed on opposite sides of the animal with the annihilation photons from the positron emission detected in coincidence. The system also includes a microCT system having a microfocus x-ray tube and an amorphous selenium detector coupled to a flat-panel readout array of thin-film resistors [182]. The same group also has developed a novel microCT scanner based on photodiode detectors that has a flexible C-arm gantry design with adjustable detector positioning, which was integrated with the microPET II scanner [66,183]. Among the objectives set were the possibility of PET

scanning with high sensitivity and high spatial resolution combined with low-dose CT to provide an image quality suitable for anatomic localization and correction of attenuation [180].

The LabPET scanner developed by the group from the University of Sherbrooke and brought to market by Gamma Medica-Ideas, Inc., is being enhanced by the addition of an advanced CT capability that allows anatomic images to be acquired using the same detector channels and electronics. PET and CT scanning can be performed simultaneously. Individual x-ray photons can be discriminated and counted in CT mode [44,179] by sampling the analog signal using high-speed analog-to-digital converters and digital processing in field-programmable gate arrays. The parallel architecture and fast digital processing allow high count rates for both PET and CT modes, whereas the modularity of the system design allows the number of channels to be extended up to 10^4 or more.

Sensitive cooled charge-coupled device cameras, which detect emitted light from fluorescent/bioluminescent probes within a living organism, have shown their potential in imaging pathologic changes in murine models of human disease (eg, infection, cancer) [140]. A few research groups are pursuing the goal of combining tomographic bioluminescence and radionuclide emission imaging to record optical and emission tomography signals [140,156,157,171,184,185]. One such design is the combined optical-PET system being explored by the group from UCLA, in which the scintillation crystal array plays the dual role of coupling the optical signal from bioluminescence/fluorescence to the photodetector and of channeling optical scintillations created from the annihilation photon interactions [156,157]. The PET scanner consists of a hexagonal configuration of six detector blocks with an inner radius of 15.6 mm. Each detector consists of a 2D array of 8×8 scintillation crystals, each measuring $2 \times 2 \times 10$ mm 3 , read out by multichannel PMTs [184,186]. Extensive Monte Carlo simulations were performed to study the feasibility of the concept and assess the effect of various geometric parameters on the performance characteristics of the system [185]. The simulation results were useful for identifying methodological challenges that need to be addressed before the practical realization of the system can be achieved.

A combined MR/diffuse OI system for dual-modality imaging of small animals was developed by integrating a multispectral frequency domain diffuse optical tomography system with a 4T MR imaging system [158]. This integration is achieved by incorporating a fiber adaptive interface inside the MR magnet. A special probe design using external fiducial markers allows accurate image registration

to be performed. The diffusion equation is worked out through a finite-element algorithm guided by a priori knowledge gained from MR imaging.

A trimodality (SPECT/CT/OI) small-animal imaging system also is being developed at the German Cancer Research Center in Heidelberg, Germany [171,187]. The SPECT component consists of a compact detector consisting of a 2×2 array of PSPMTs connected to a 66×66 array of opto-decoupled $1.3 \times 1.3 \times 6$ -mm 3 thallium-doped sodium iodide crystals. The optical subsystem consists of a high-resolution charge-coupled device (CCD) camera containing a progressive-scan interline CCD chip. Various laser sources, selected by wavelength and light power requirements, can be mounted on the gantry. The CT component uses an x-ray tube having a 35- μm focal spot size and a cone angle of 24° , whereas the x-ray detector consists of a 49.2×98.6 -mm 2 gadolinium oxide sulfide (Gd₂O₂S) scintillator screen placed in direct contact with a complementary metal oxide semiconductor (CMOS) photodiode array with a sensor pixel size of 48 μm . The modular design allows the subsystems to be mounted on a common gantry, thus enabling a wide range of applications to be performed.

Early attempts to design MR-compatible PET units were made at the University of Minnesota in the 1990s [188–190]. This effort was followed by a close collaboration between UCLA and Guys and St. Thomas Hospital, London [160,161]. It soon was realized that several important challenges must be overcome in implementing and operating a combined PET/MR imaging system using conventional PET detectors. Virtually all clinical PET detectors use PMTs whose performance can be seriously affected in the presence of magnetic fields significantly smaller than those produced by modern MR imaging scanners. This interaction is especially problematic in an MR imaging scanner that relies on rapidly switching gradient magnetic fields and radiofrequency (RF) signals to produce the MR image. The presence of the magnetic field gradients and RF signals certainly could disrupt the performance of a PMT and PET detector if they were located within or adjacent to the magnet of the MR imaging system. Similarly, the operation of the MR imaging system relies on a very uniform and stable magnetic field to produce the MR image. The introduction of radiation detectors, electronics, and other bulk materials can perturb the magnetic field and RF pulses in a way that introduces artifacts in the MR image.

Despite these challenges, several research groups are investigating ways to integrate a PET system directly in an MR imaging scanner by designing detectors made from nonmagnetic materials that

can be placed within the magnetic field of an MR imaging/MR spectroscopy system. A few European (University of Tübingen, Germany, and the University of Cambridge, UK) and several North American (California Institute of Technology and UC Davis; West Virginia University; Jefferson Lab in Newport News, Virginia; Stanford University; Brookhaven National Laboratory; and the University of Western Ontario) institutions are active in the field, and there are clear indications that large companies in the United States (apart from Siemens Medical Solutions) are developing innovative approaches for combined PET/MR imaging. For example, the UCLA group developed a 3.8-cm ring of small scintillator crystals that was placed in the MR imaging system for PET imaging [160,161]. The crystals were optically coupled through 3-m-long fiber optics to an external array of position-sensitive photomultiplier tubes and could be read out through external processing electronics. By keeping the radiation-sensitive elements of the detector within the MR system, and operating the detectors and electronics away from the magnetic field, the combined system could perform simultaneous PET/MR imaging without measurable mutual interaction effects. The same group also performed simultaneous PET/MR imaging with a larger detector ring (5.6 cm in diameter) using the same design [160,161]. Their collaborators at Kings College, London, placed the system inside a 9.4-T nuclear magnetic resonance (NMR) spectrometer to study metabolism in an isolated, perfused rat heart model. ^{32}P -NMR spectra were acquired simultaneously with PET images of ^{18}F -fluorodeoxyglucose (FDG) uptake in the myocardium [191,192]. The investigators planned to extend this concept to develop an MR-compatible PET scanner with one ring of 480 LSO crystals arranged in three layers (160 crystals per layer) with a diameter of 11.2 cm corresponding to a FoV 5 cm, large enough to accommodate an animal within a stereotactic frame [160]. The light loss through a fiber 3.25 m long was reported to be close to 70% [162] and to be approximately 90% for a length of 2.5 m [168]. It is argued, however, that the number of scintillation photons is sufficient to determine the position of interaction within the detector block accurately. As reported by Zaidi and Alavi [193], other approaches based on conventional PMT-based readout and conventional PET detectors use either the same principles [166,194] or rely on more complex magnet designs, including a split magnet [164] or field-cycled MR imaging [195].

More recently, other investigators have proposed PET/MR imaging systems configured with suitable solid-state detectors that are insensitive to magnetic fields and consequently can be operated within

a magnetic field for PET imaging. Some groups have tested APDs and silicon PMTs (SiPMs) within a high magnetic field and have produced PET and MR images that seem to be free of severe artifacts and distortion [163,165,170]. Silicon PMTs are good candidates for the design of combined PET/MR scanners [196] because they allow a significant reduction in the electronics required inside the MR imaging device [197].

The latest version of the PET/MR system developed at the University of Tübingen (Fig. 15), following major improvements of the initial design [163], consists of detector modules comprising a 12×12 LSO scintillator array ($1.6 \times 1.6 \times 4.5 \text{ mm}^3$), a 3×3 APD array, and custom charge-sensitive preamplifier electronics, located within a thin copper-shielded housing [165]. The multiring PET scanner comprises a total of 10 LSO-APD detector modules with an axial and transaxial FoV of 19 mm and 40 mm, respectively, to produce 23 slices with a slice thickness of approximately 0.8 mm. The signals emanating from the 10 detector modules are read out and processed with dedicated PET electronics (Siemens Medical Solutions, Knoxville, Tennessee). The housing was designed to reduce potential interference with basic components of the 7-T ClinScan animal MR imaging scanner (Bruker BioSpin MRI, Billerica, MA) including the magnetic field, field gradients, and RF receiver/transmitter electronics. The PET insert is introduced between the gradient and the 35-mm RF coil of the MR imaging scanner (30-cm bore). The functional FoV of the combined PET/MR imaging system is 19 mm in the axial direction (limited by the detector modules of the PET subsystem) and 35 mm in transaxial direction (limited by the diameter of the RF coil). Nevertheless, the FoV is large enough to allow imaging an entire mouse brain/heart or even large tumors of mice or small rats. There is no mutual interference between PET and MR imaging when operated simultaneously, even when more demanding MR sequences such as echo planar imaging are used for functional MR imaging [165,198]. Moreover, NMR spectroscopy is feasible in parallel with PET data acquisition [194,198].

A contemporaneous PET/MR imaging scanner based on the technology used for the newer version of the Rat Conscious Animal PET (RATCAP), a complete 3D tomograph designed to image the brain of an awake rat [199], that incorporates the PET system into an integrated, compact arrangement of LSO/APD arrays with highly integrated electronics is being developed at Lawrence Berkeley National Laboratories [200]. The PET detector modules would be positioned around the exterior of the RF pickup coil of the MR imaging scanner. The system would

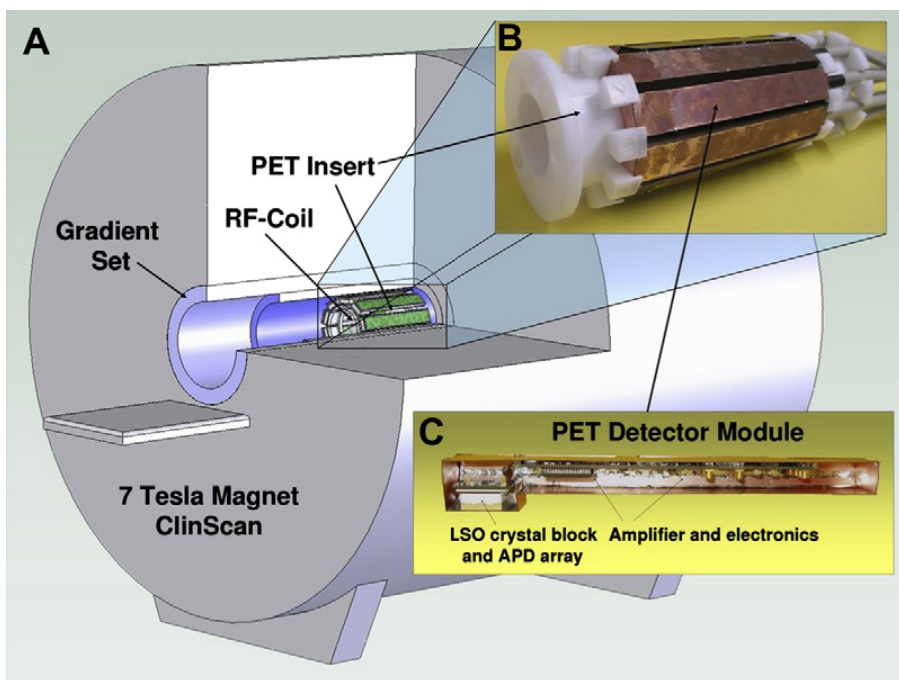


Fig. 15. Combined small-animal PET/MR imaging developed by the University of Tübingen (Germany). The PET insert is fully integrated into a 7-T MR imaging system (ClinScan, Bruker). (A) PET/MR imaging combination, showing the PET insert placed inside the MR imaging scanner, matching the centers of both FOVs. (B) The MR imaging-compatible PET insert, consisting of 10 detector modules. (C) Single PET detector module showing the LSO scintillator block, APD array, and preamplifier built into a MR imaging-compatible copper shielding. The system showed excellent performance without noticeable mutual interference between the two modalities. (From Judenhofer MS, Wehr HF, Newport DF, et al. Simultaneous PET/MRI: a new perspective for functional and morphological imaging. *Nature Medicine* 2008; in press; with permission.)

be configured to fit within a radial distance of approximately 3 to 4 cm outside the RF coil and would be arranged to have a fairly small number of cables pending out of the bore of the MR imaging scanner.

There is still scope for innovative designs of combined PET/MR units, and, given the enthusiasm and creativity of the groups involved, the future of this technology is undoubtedly bright [201].

Quantification of small-animal PET data

Quantification provides the direct relationship between the activity concentration measured *in vivo* in organs/tissues and the underlying physiologic or pharmacokinetic processes occurring in the structure of interest [202]. It links the variation in the activity concentration over time to physiologically relevant quantitative parameters such as the regional cerebral glucose metabolism (rCGM), regional cerebral blood flow, or concentrations of receptors or other binding sites. Absolute quantification generally requires accurate measurement of activity concentrations in arterial blood, which provides the input function to the kinetic model using more advanced blood sampling devices [203,204], although blood sampling-free techniques that rely on population-based input functions, extraction of the input functions from the images, and other more complex approaches are being explored by several groups [205]. The common goal of these

techniques is to develop tools for producing quantitative regional estimates of physiologic or pharmacokinetic parameters from dynamic radiotracer studies. These techniques are reviewed elsewhere in this issue by Bentourquia and Zaidi [206] and are not repeated here. To take full advantage of the quantitative capabilities of PET imaging, data normalization [133,134,207] and object-specific correction of background (randoms) and physical degrading factors such as attenuation [208], scatter [101], partial volume [99], and motion [209], must be performed before reconstruction or incorporated within advanced iterative image reconstruction techniques.

Within the particular context of small-animal imaging, many aspects need to be addressed when image quantification is the target. Among these considerations are animal handling and preparation [210], the mode and type of anesthesia administered [211], and the mass of the injected tracer [212]. Anesthesia generally is used to eliminate motion artifacts during scanning, but it strongly affects the neurologic state of the animal and precludes the use of PET to study the brain during normal behavior in the usual living environment of the animal [199,211]. The effect of dietary conditions, mode of anesthesia, and ambient temperature on the biodistribution of ¹⁸F-FDG and tumor glucose metabolism in mice was assessed with the aim of proposing PET scanning protocols that optimize visualization of tumor xenografts [210]. It was

found that fasting and warming the animals before injection and during the uptake period significantly improved tumor visualization. Likewise, anesthesia should be selected carefully for tumor-bearing mice [210] and for absolute quantification of rCGM [213]. Moreover, computation of rCGM from ¹⁸F-FDG data in hyperglycemic animals may require alternative rate and lumped constants [213]. It also has been demonstrated that if the specific activity of some tracers and/or the sensitivity of small-animal PET scanners are not improved compared with clinical studies, small-animal imaging will not depict the “true” tracer distribution accurately [212]. This is particularly true in the case of low-density binding sites such as receptors where the increased mass injected might saturate the receptor and lead to physiologic effects and nonlinear kinetics.

Several studies reported on the assessment of the quantitative capability of small-animal PET studies [207,213–217]. For example, Fahey and colleagues [214] reported that the microPET P4 scanner provides accurate quantitation to within 6% for features larger than 10 mm. In addition, 60% of object contrast was preserved for features as small as 4 mm. The development of tracer-specific small-animal PET probabilistic atlases [218] correlated with anatomic (eg, MR imaging) templates will enable automated volume-of-interest or voxel-based analysis of small-animal PET data with minimal end-user interaction [219]. One such software tool was developed by Kesner and colleagues [215] to enable the assessment of the biodistribution of PET tracers using small-animal PET data. This assessment is achieved through nonrigid coregistration of a digital mouse phantom with the animal PET image followed by automated calculation of tracer concentrations in 22 predefined volumes of interest representing the whole body and major organs. The development of advanced anatomic models including both stylized and more realistic voxel-based mouse [220–223] and rat [224] models obtained from serial cryosections or dedicated high-resolution small-animal CT scanners will help to support ongoing research in this area [225].

Biomedical applications of preclinical PET

During the first days of their inception, the role of small-animal PET scanners was rather unclear and controversial [226]. It later was recognized with a more pronounced enthusiasm that this technology is essential for molecular imaging-based biomedical research [29,227,228]. The limited number of studies involving small-animal imaging on large-bore clinical PET scanners has established

clearly the need for dedicated small-animal PET units, particularly to enhance the detectability of small tumors in tumor-bearing mice [229,230]. An impressive literature exists on the use of PET in animal research, ranging from the mouse up to the monkey. A comprehensive overview of published literature is beyond the scope of this article. Dedicated high-resolution small-animal PET scanners have been used in a wide variety of fields including tracer development [231,232], drug discovery [233–236], development of therapeutic targets and targeted therapies [237,238], and many other applications [239].

Murine models now have an essential role in formulating modern concepts of mammalian biology and human disease and provide biomedical researchers with a realistic means of developing and evaluating new diagnostic and therapeutic techniques [6,240,241]. In addition, transgenic and knockout techniques now are available for manipulating the genome in a way that allows biologists to tailor animal models that accurately recapitulate biologic and biochemical processes in the human. Mouse models now are available that allow investigators to study the development of tumors in mice in a way that represents virtually all major human cancers, including those of the lung [242,243], gastrointestinal system [244,245], nervous system [246], breast [247,248], liver [249], prostate [250,251], pancreas [252], reproductive system [253], and metastases [149]. Similarly, in cardiovascular research [254–256], animal models are important for studying the hormonal pathways involved in the regulation of hypertension and hypertension therapy [257,258], cardiac electrophysiology [259,260], mechanisms of apoptosis [249,261], effects of exercise [262], lipid metabolism and insulin sensitivity [263,264], atherosclerosis [265,266], and angiogenesis [265,267]. Likewise, the prospective impact of molecular imaging in many aspects of neuroscience research is well established [268]. The role of transgenic and knockout mice in biomedical research now has become profound and widespread, and transgenic animals (mice and rats) now can be designed and created in a way that offers almost unlimited possibilities for addressing questions concerning the genetic, molecular, and cellular basis of biology and disease [240,269,270].

With the ever-increasing number and importance of human disease models, particularly in rodents (mice and rats) [240,269,270], the potential of high-resolution PET instrumentation to contribute unique information is becoming apparent to many researchers. Radionuclide imaging can be performed using *in vitro* autoradiography. This technology offers exquisite spatial resolution but is extremely

time consuming and labor intensive, particularly when large volumes of tissue need to be sliced, exposed, and digitized. Unlike autoradiography, however, PET can deliver functional and kinetic data from large volumes of tissue (in some cases the entire animal), with results available within minutes of the end of the study. PET also offers the critical advantage of providing functional information non-invasively, so each animal can be studied repeatedly. Thus each animal can serve as its own control in studies with a longitudinal design. Some animal models (particularly those involving pharmacologic or surgical intervention) can exhibit high variability from one animal to another, thereby strongly supporting study designs in which disease progression or therapeutic response must be followed in an individual animal. The development of animal models often involves a large investment in time and expertise (particularly for transgenic animals and study of gene therapy protocols). In these cases, researchers would welcome a tool that can assess biologic function noninvasively to reduce study costs and to improve statistical power with limited numbers of animals because an individual animal can serve as its own control.

The use of PET for biologic research in small animals presents several challenges beyond those faced in clinical faculties. First, small-animal imaging typically is used in a research laboratory rather than a medical clinic. Therefore, the PET unit should be reliable, easy to use, and relatively low cost. Second, small-animal PET imaging must achieve millimeter, and ideally submillimeter, spatial resolution to detect small lesions including micrometastases. Finally, a high level of detection efficiency is needed to allow procedures to be completed within the 1 hour during which the animal can be anesthetized safely. Excellent detection efficiency also minimizes the amount of radiopharmaceutical needed for the study and limits the radiation dose.

The radiation dose delivered to animals is one of the critical issues in preclinical imaging. It can be very high, depending on the experiment, and should be monitored carefully because it might change tumor characteristics, induce significant biologic effects (thus changing the animal model being studied), or even cause death [271,272]. The same caveats apply to other imaging modalities such as CT [223], particularly when performed using multimodality imaging systems in which the resulting absorbed dose is the sum of the individual contributions of each modality. Although much worthwhile effort has been devoted toward the assessment of the radiation dose delivered to human subjects, few research studies have addressed this issue for small animals [223,224,271,273].

Summary and future directions

PET technology has not yet reached its performance potential. There are still substantial improvements to be made in the ability to visualize and quantify subtle signatures associated with molecular-based disease processes within a population of cells residing inside a living subject. This article has focused on describing the challenges faced by preclinical high-resolution PET system design and a number of new technologies under investigation. If successful, these advances will improve PET's ability to visualize and quantify low concentrations of the desired signal.

The basic system performance parameters that have been targeted for improvement are photon sensitivity, spatial resolution, energy resolution, and coincidence time resolution. The latter two parameters affect the contrast and contrast resolution, and all performance parameters affect the attainable molecular sensitivity.

If successful, the imaging system technologies described in this article could lead to an order-of-magnitude increase in the molecular sensitivity of PET. If this hypothetical order-of-magnitude enhancement in molecular sensitivity were implemented in a preclinical PET system, it would enable the measurement of lower concentrations of signal associated with new probes, targets, and assays under study to understand and quantify subtle signatures of molecular-based disease processes and to guide the discovery and development of novel molecular-based treatments. In the clinic, such new technologies would be important to enable physicians to visualize and quantify smaller congregations of diseased cells emitting signal, which could impact the detection of earlier signatures of disease or its recurrence.

Acknowledgments

C.S. Levin would like to acknowledge the scientists and engineers from Radiation Monitoring Devices, Inc. (Watertown, Massachusetts), in particular Richard Farrell, for help with designing, developing, and studying the described new thin PSAPD detectors; the scientists and engineers from the University of California, San Diego Center for Astrophysics and Space Research, in particular James Matteson, for help with designing, developing, and studying the described prototype cross-strip CZT detectors; present and past student, postdoctoral, and staff colleagues in the Molecular Imaging Instrumentation Laboratory at Stanford, such as Peter Olcott, Garry Chinn, Guillem Pratx, Angela Foudray, Frezghi Habte, and Jin Zhang, for

their significant contributions to the work described and referenced in this article; and Sanjiv Gambhir for his support and encouragement of this work performed within the Molecular Imaging Program at Stanford.

References

- [1] Gambhir SS. Molecular imaging of cancer with positron emission tomography. *Nat Rev Cancer* 2002;2:683–93.
- [2] Haubner R, Weber WA, Beer AJ, et al. Noninvasive visualization of the activated alphavbeta3 integrin in cancer patients by positron emission tomography and [18F]Galacto-RGD. *PLoS Med* 2005;2:e70.
- [3] Vavere AL, Welch MJ. Preparation, biodistribution, and small animal PET of 45Ti-transferrin. *J Nucl Med* 2005;46:683–90.
- [4] McQuade P, Martin KE, Castle TC, et al. Investigation into 64Cu-labeled Bis(selenosemicarbazone) and Bis(thiosemicarbazone) complexes as hypoxia imaging agents. *Nucl Med Biol* 2005;32:147–56.
- [5] Robinson MK, Doss M, Shaller C, et al. Quantitative immuno-positron emission tomography imaging of HER2-positive tumor xenografts with an iodine-124 labeled anti-HER2 diabody. *Cancer Res* 2005;65:1471–8.
- [6] Lyons SK. Advances in imaging mouse tumour models in vivo. *J Pathol* 2005;205:194–205.
- [7] Waldherr C, Mellinghoff IK, Tran C, et al. Monitoring antiproliferative responses to kinase inhibitor therapy in mice with 3'-deoxy-3'-18F-fluorothymidine PET. *J Nucl Med* 2005;46:114–20.
- [8] Thakur ML, Aruva MR, Gariepy J, et al. PET imaging of oncogene overexpression using 64Cu-vasoactive intestinal peptide (VIP) analog: comparison with 99mTc-VIP analog. *J Nucl Med* 2004;45:1381–9.
- [9] Aliaga A, Rousseau JA, Cadorette J, et al. A small animal positron emission tomography study of the effect of chemotherapy and hormonal therapy on the uptake of 2-Deoxy-2-[F-18]fluoro-D-glucose in murine models of breast cancer. *Mol Imaging Biol* 2007;9:144–50.
- [10] Barthel H, Wilson H, Collingridge DR, et al. In vivo evaluation of [18F]fluoroetanidazole as a new marker for imaging tumour hypoxia with positron emission tomography. *Br J Cancer* 2004;90:2232–42.
- [11] Sundaresan G, Yazaki PJ, Shively JE, et al. 124I-labeled engineered anti-CEA minibodies and diabodies allow high-contrast, antigen-specific small-animal PET imaging of xenografts in athymic mice. *J Nucl Med* 2003;44:1962–9.
- [12] Solomon B, McArthur G, Cullinane C, et al. Applications of positron emission tomography in the development of molecular targeted cancer therapeutics. *BioDrugs* 2003;17:339–54.
- [13] Yang H, Berger F, Tran C, et al. MicroPET imaging of prostate cancer in LNCAP-SR39TK-GFP mouse xenografts. *Prostate* 2003;55:39–47.
- [14] Ray P, Pimenta H, Paulmurugan R, et al. Noninvasive quantitative imaging of protein-protein interactions in living subjects. *Proc Natl Acad Sci U S A* 2002;99:3105–10.
- [15] Luker GD, Sharma V, Pica CM, et al. Noninvasive imaging of protein-protein interactions in living animals. *Proc Natl Acad Sci U S A* 2002;99:6961–6.
- [16] Luker GD. Special conference of the American Association for Cancer Research on molecular imaging in cancer: linking biology, function, and clinical applications in vivo. *Cancer Res* 2002;62:2195–8.
- [17] Adonai N, Nguyen KN, Walsh J, et al. Ex vivo cell labeling with 64Cu-pyruvaldehyde-bis(N4-methylthiosemicarbazone) for imaging cell trafficking in mice with positron-emission tomography. *Proc Natl Acad Sci U S A* 2002;99:3030–5.
- [18] Wang J, Maurer L. Positron emission tomography: applications in drug discovery and drug development. *Curr Top Med Chem* 2005;5:1053–75.
- [19] Frangioni JV, Hajjar RJ. In vivo tracking of stem cells for clinical trials in cardiovascular disease. *Circulation* 2004;110:3378–83.
- [20] Cao F, Lin S, Xie X, et al. In vivo visualization of embryonic stem cell survival, proliferation, and migration after cardiac delivery. *Circulation* 2006;113:1005–14.
- [21] Blasberg RG, Tjuvajev JG. Molecular-genetic imaging: current and future perspectives. *J Clin Invest* 2003;111:1620–9.
- [22] Pither R. PET and the role of in vivo molecular imaging in personalized medicine. *Expert Rev Mol Diagn* 2003;3:703–13.
- [23] Shah K, Jacobs A, Breakefield XO, et al. Molecular imaging of gene therapy for cancer. *Gene Ther* 2004;11:1175–87.
- [24] Wu JC, Inubushi M, Sundaresan G, et al. Positron emission tomography imaging of cardiac reporter gene expression in living rats. *Circulation* 2002;106:180–3.
- [25] Jacobs A, Voges J, Reszka R, et al. Positron-emission tomography of vector-mediated gene expression in gene therapy for gliomas. *Lancet* 2001;358:727–9.
- [26] Inubushi M, Wu JC, Gambhir SS, et al. Positron-emission tomography reporter gene expression imaging in rat myocardium. *Circulation* 2003;107:326–32.
- [27] Hnatowich DJ. Observations on the role of nuclear medicine in molecular imaging. *J Cell Biochem Suppl* 2002;39:18–24.
- [28] Chakrabarti A, Zhang K, Aruva MR, et al. Radio-hybridization PET imaging of KRAS G12D mRNA expression in human pancreas cancer xenografts with [(64)Cu]DO3A-peptide nucleic

- acid-peptide nanoparticles. *Cancer Biol Ther* 2007;6:948–56.
- [29] Tai YC, Lafosse R. Instrumentation aspects of animal PET. *Annu Rev Biomed Eng* 2005;7: 255–85.
- [30] Ingvar M, Eriksson L, Rogers GA, et al. Rapid feasibility studies of tracers for positron emission tomography: high-resolution PET in small animals with kinetic analysis. *J Cereb Blood Flow Metab* 1991;11:926–31.
- [31] Fowler JS, Volkow ND, Wolf AP, et al. Mapping cocaine binding sites in human and baboon brain in vivo. *Synapse* 1989;4:371–7.
- [32] Agon P, Kaufman JM, Goethals P, et al. Study with positron emission tomography of the osmotic opening of the dog blood-brain barrier for quinidine and morphine. *J Pharm Pharmacol* 1988;40:539–43.
- [33] Cutler PD, Cherry SR, Hoffman EJ, et al. Design features and performance of a PET system for animal research. *J Nucl Med* 1992;33:595–604.
- [34] Watanabe M, Uchida H, Okada H, et al. A high resolution PET for animal studies. *IEEE Trans Med Imaging* 1992;11:577–80.
- [35] Malakoff D. The rise of the mouse, biomedicine's model mammal. *Science* 2000;288: 248–53.
- [36] Marshall E. Genome sequencing. Celera assembles mouse genome; public labs plan new strategy. *Science* 2001;292:822.
- [37] Nadeau JH, Balling R, Barsh G, et al. Sequence interpretation. Functional annotation of mouse genome sequences. *Science* 2001;291:1251–5.
- [38] Bloomfield PM, Rajeswaran S, Spinks TJ, et al. The design and physical characteristics of a small animal positron emission tomograph. *Phys Med Biol* 1995;40:1105–26.
- [39] Jeavons A, Kull K, Lindberg B, et al. A proportional chamber positron camera for medical imaging. *Nuclear Instruments and Methods in Physics Research A* 1980;176:89–97.
- [40] Cherry SR, Shao Y, Silverman RW, et al. Micro-PET: a high resolution PET scanner for imaging small animals. *IEEE Trans Nucl Sci* 1997;44: 1161–6.
- [41] Seidel J, Vaquero JJ, Green MV. Resolution uniformity and sensitivity of the NIH ATLAS small animal PET scanner: comparison to simulated LSO scanners without depth-of-interaction capability. *IEEE Trans Nucl Sci* 2003;50:1347–50.
- [42] Surti S, Karp JS, Perkins AE, et al. Design evaluation of A-PET: a high sensitivity animal PET camera. *IEEE Trans Nucl Sci* 2003;50: 1357–63.
- [43] Uribe J, Li H, Xing T, et al. Signal characteristics of individual crystals in high resolution BGO detector designs using PMT-quadrant sharing. *IEEE Trans Nucl Sci* 2003;50:355–61.
- [44] Fontaine R, Belanger F, Cadorette J, et al. Architecture of a dual-modality, high-resolution, fully digital positron emission tomography/computed tomography (PET/CT) scanner for small animal imaging. *IEEE Trans Nucl Sci* 2005;52:691–6.
- [45] Del Guerra A, Bartoli A, Belcari N, et al. Performance evaluation of the fully engineered YAP-(S)PET scanner for small animal imaging. *IEEE Trans Nucl Sci* 2006;53:1078–83.
- [46] Ziemons K, Auffray E, Barbier R, et al. The ClearPET™ project: development of a 2nd generation high-performance small animal PET scanner. *Nuclear Instruments and Methods in Physics Research A* 2005;537:307–11.
- [47] Knoxville TN. Siemens preclinical solutions I. Available at: <http://www.medical.siemens.com/>; 2007. Accessed October, 2007.
- [48] GE-Suinsa. Madrid (Spain). Available at: <http://www.gehealthcare.com/preclinical>; 2007.
- [49] Philips Medical Systems. Andover, MA. Available at: <http://www.medical.philips.com/main/products/preclinical/>; 2007. Accessed October, 2007.
- [50] Gamma Medica-Ideas. Northridge, CA. Available at: <http://www.gm-ideas.com/>; 2007. Accessed October, 2007.
- [51] Ingegneria dei Sistemi Elettronici. Pisa (Italy). Available at: <http://www.ise-srl.com/YAPPET/>; 2007. Accessed October, 2007.
- [52] Raytest GmbH. Straubenhardt (Germany). Available at: <http://www.raytest.de/>; 2007. Accessed October, 2007.
- [53] Oxford Positron Systems Ltd. Oxford (UK). Available at: <http://www.oxpos.co.uk/>; 2007. Accessed October, 2007.
- [54] Wang Y, Seidel J, Tsui BM, et al. Performance evaluation of the GE Healthcare eXplore VISTA dual-ring small-animal PET scanner. *J Nucl Med* 2006;47:1891–900.
- [55] Surti S, Karp JS, Perkins AE, et al. Imaging performance of a-PET: a small animal PET camera. *IEEE Trans Med Imaging* 2005;24:844–52.
- [56] Huisman MC, Reder S, Weber AW, et al. Performance evaluation of the Philips MOSAIC small animal PET scanner. *Eur J Nucl Med Mol Imaging* 2007;34:532–40.
- [57] Dumouchel T, Bergeron M, Cadorette J, et al. Initial performance assessment of the LabPET APD-based digital PET scanner [abstract]. *J Nucl Med* 2007;48:39.
- [58] Jeavons AP, Chandler RA, Dettmar CAR. A 3D HIDAC-PET camera with sub-millimetre resolution for imaging small animals. *IEEE Trans Nucl Sci* 1999;46:468–73.
- [59] Missimer J, Madi Z, Honer M, et al. Performance evaluation of the 16-module quad-HIDAC small animal PET camera. *Phys Med Biol* 2004;49:2069–81.
- [60] Schafers KP, Reader AJ, Kriens M, et al. Performance evaluation of the 32-module quadHIDAC small-animal PET scanner. *J Nucl Med* 2005;46:996–1004.
- [61] Habte F, Foudray AMK, Olcott PD, et al. Effects of system geometry and other physical factors

- on photon sensitivity of high-resolution positron emission tomography. *Phys Med Biol* 2007;52:3753–72.
- [62] Parnham KB, Chowdhury S, Li J, et al. Second-generation, tri-modality pre-clinical imaging system. In: Phlips B, editor. IEEE Nuclear Science Symposium Conference Record 2007. Piscataway, NJ.
- [63] Levin CS, Hoffman EJ. Calculation of positron range and its effect on the fundamental limit of positron emission tomography system spatial resolution. *Phys Med Biol* 1999;44:781–99 Corrigendum: *Phys Med Biol* 2000;45:559.
- [64] Phelps ME, Huang SC, Hoffman EJ, et al. An analysis of signal amplification using small detectors in positron emission tomography. *J Comput Assist Tomogr* 1982;6:551–65.
- [65] Miyaoka RS, Kohlmyer SG, Lewellen TK. Performance characteristics of micro crystal element (MiCE) detectors. *IEEE Trans Nucl Sci* 2001;48:1403–7.
- [66] Tai Y-C, Chatzioannou A, Yang Y, et al. Micro-PET II: design, development and initial performance of an improved microPET scanner for small-animal imaging. *Phys Med Biol* 2003;48:1519–37.
- [67] Cherry SR, Shao Y, Tornai MP, et al. Collection of scintillation light from small BGO crystals. *IEEE Trans Nucl Sci* 1995;42:1058–63.
- [68] Levin CS. Design of a high-resolution and high-sensitivity scintillation crystal array for PET with nearly complete light collection. *IEEE Trans Nucl Sci* 2002;49:2236–43.
- [69] Ordóñez CE, Matthews KL II, et al. Rebinning errors in coincidence imaging due to depth of interaction. *IEEE Trans Nucl Sci* 2001;48:1386–90.
- [70] Qi J, Leahy RM, Cherry SR, et al. High-resolution 3D Bayesian image reconstruction using the microPET small-animal scanner. *Phys Med Biol* 1998;43:1001–13.
- [71] Reader AJ, Zaidi H. Advances in PET image reconstruction. *PET Clinics* 2(2); in press.
- [72] Zhang J, Olcott PD, Chinn G, et al. Study of the performance of a novel 1 mm resolution dual-panel PET camera design dedicated to breast cancer imaging using Monte Carlo simulation. *Med Phys* 2007;34:689–702.
- [73] Brasse D, Kinahan PE, Clackdoyle R, et al. Fast fully 3-D image reconstruction in PET using planograms. *IEEE Trans Med Imaging* 2004;23:413–25.
- [74] Lewitt RM, Matej S. Overview of methods for image reconstruction from projections in emission computed tomography. Proceedings of the IEEE 2003;91:1588–611.
- [75] Defrise M, Kinahan PE, Townsend DW, et al. Exact and approximate rebinning algorithms for 3-D PET data. *IEEE Trans Med Imaging* 1997;16:145–58.
- [76] Vandenbergh S, Daube-Witherspoon ME, Lewitt RM, et al. Fast reconstruction of 3D time-of-flight PET data by axial rebinning and transverse mashing. *Phys Med Biol* 2006;51:1603–21.
- [77] Liu X, Comtat C, Michel C, et al. Comparison of 3-D reconstruction with 3D-OSEM and with FORE+OSEM for PET. *IEEE Trans Med Imaging* 2001;20:804–14.
- [78] Rahmim A, Lenox M, Reader AJ, et al. Statistical list-mode image reconstruction for the high resolution research tomograph. *Phys Med Biol* 2004;49:4239–58.
- [79] Rahmim A, Cheng J-C, Blinder S, et al. Statistical dynamic image reconstruction in state-of-the-art high-resolution PET. *Phys Med Biol* 2005;50:4887–912.
- [80] Asma E, Nichols TE, Qi J, et al. 4D PET image reconstruction from list mode data. IEEE Nuclear Science Symposium Conference Record 2000;2:15/57–15/65.
- [81] Walledge RJ, Reader AJ, Aboagye EO, et al. 4D PET with the quad-HIDAC: development of dynamic list-mode EM image reconstruction. IEEE Nuclear Science Symposium Conference Record 2002;3:1716–20.
- [82] Huesman RH, Klein GJ, Moses WW, et al. List-mode maximum-likelihood reconstruction applied to positron emission mammography (PEM) with irregular sampling. *IEEE Trans Med Imaging* 2000;19:532–7.
- [83] Reader AJ, Erlandsson K, Flower MA, et al. Fast accurate iterative reconstruction for low-statistics positron volume imaging. *Phys Med Biol* 1998;43:835–46.
- [84] Parra L, Barrett HH. List-mode likelihood: EM algorithm and image quality estimation demonstrated on 2-D PET. *IEEE Trans Med Imaging* 1998;17:228–35.
- [85] Verhaeghe J, D'Asseler Y, Vandenberghe S, et al. An investigation of temporal regularization techniques for dynamic PET reconstructions using temporal splines. *Med Phys* 2007;34:1766–78.
- [86] Reader AJ, Ally S, Bakatselos F, et al. One-pass list-mode EM algorithm for high-resolution 3-D PET image reconstruction into large arrays. *IEEE Trans Nucl Sci* 2002;49:693–9.
- [87] Rehfeld N, Alber M. A parallelizable compression scheme for Monte Carlo scatter system matrices in PET image reconstruction. *Phys Med Biol* 2007;52:3421–37.
- [88] Joseph PM. An improved algorithm for reprojecting rays through pixel images. *IEEE Trans Med Imaging* 1982;1:192–6.
- [89] Siddon R. Fast calculation of the exact radiological path for 3-D CT. *Med Phys* 1985;12:252–5.
- [90] Alessio AM, Kinahan PE. Improved quantitation for PET/CT image reconstruction with system modeling and anatomical priors. *Med Phys* 2006;33:4095–103.
- [91] Herranz JL, España S, Vaquero JJ, et al. FIRST: fast iterative reconstruction software for (PET) tomography. *Phys Med Biol* 2006;51:4547–65.

- [92] Mumcuoglu EU, Leahy RM, Cherry SR, et al. Accurate geometric and physical response modelling for statistical image reconstruction in high resolution PET. Conference Record IEEE Nuclear Science Symposium 1996;3:1569–73.
- [93] Rafecas M, Mosler B, Dietz M, et al. Use of a Monte Carlo-based probability matrix for 3-D iterative reconstruction of MADPET-II data. IEEE Trans Nucl Sci 2004;51:2597–605.
- [94] Markiewicz PJ, Tamal M, Julyan PJ, et al. High accuracy multiple scatter modelling for 3D whole body PET. Phys Med Biol 2007;52:829–47.
- [95] Panin VY, Kehren F, Rothfuss H, et al. PET reconstruction with system matrix derived from point source measurements. IEEE Trans Nucl Sci 2006;53:152–9.
- [96] Panin VY, Kehren F, Michel C, et al. Fully 3-D PET reconstruction with system matrix derived from point source measurements. IEEE Trans Med Imaging 2006;25:907–21.
- [97] Phelps M. PET: molecular imaging and its biological applications. New York: Springer-Verlag Inc.; 2004.
- [98] Hoffman EJ, Huang SC, Phelps ME. Quantitation in positron emission computed tomography: 1. Effect of object size. J Comput Assist Tomogr 1979;3:299–308.
- [99] Rousset OG, Rahmim A, Alavi A, et al. Partial volume correction strategies in PET. PET Clinics 2(2); in press.
- [100] Zaidi H, Koral KE. Scatter modelling and compensation in emission tomography. Eur J Nucl Med Mol Imaging 2004;31:761–82.
- [101] Zaidi H, Montandon M. Scatter compensation techniques in PET. PET Clinics 2(2); in press.
- [102] Yang Y, Cherry SR. Observations regarding scatter fraction and NEC measurements for small animal PET. IEEE Trans Nucl Sci 2006;53:127–32.
- [103] Tornai MP, Germano G, Hoffman EJ. Positioning and energy response of PET block detectors with different light sharing schemes. IEEE Trans Nucl Sci 1994;41:1458–63.
- [104] Tai Y, Chatzioannou A, Siegel S, et al. Performance evaluation of the microPET P4: a PET system dedicated to animal imaging. Phys Med Biol 2001;46:1845–62.
- [105] Siegel S, Silverman RW, Shao Y, et al. Simple charge division readouts for imaging scintillator arrays using a multi-channel PMT. IEEE Trans Nucl Sci 1996;43:1634–41.
- [106] Brasse D, Kinahan PE, Lartizien C, et al. Correction methods for random coincidences in fully 3D whole-body PET: impact on data and image quality. J Nucl Med 2005;46:859–67.
- [107] Strother SC, Casey ME, Hoffman EJ. Measuring PET scanner sensitivity: relating countrates to image signal-to-noise ratios using noise equivalents counts. IEEE Trans Nucl Sci 1990;37:783–8.
- [108] Moses WW. Time of flight in PET revisited. IEEE Trans Nucl Sci 2003;50:1325–30.
- [109] Surti S, Karp JS, Popescu LM, et al. Investigation of time-of-flight benefit for fully 3-D PET. IEEE Trans Med Imaging 2006;25:529–38.
- [110] Conti M. Effect of randoms on signal-to-noise ratio in TOF PET. IEEE Trans Nucl Sci 2006;53:1188–93.
- [111] Budinger TF. Time-of-flight positron emission tomography: status relative to conventional PET. J Nucl Med 1983;24:73–8.
- [112] Moses WW, Derenzo SE, Melcher CL, et al. A room temperature LSO/PIN photodiode PET detector module that measures depth of interaction. IEEE Trans Nucl Sci 1995;42:1085–9.
- [113] Schmand M, Eriksson L, Casey ME, et al. Advantages using pulse shape discrimination to assign the depth of interaction information (DOI) from a multi layer phoswich detector. IEEE Trans Nucl Sci 1999;46:985–90.
- [114] Streun M, Brandenburg G, Larue H, et al. Pulse shape discrimination of LSO and LuYAP scintillators for depth of interaction detection in PET. IEEE Trans Nucl Sci 2003;50:344–7.
- [115] Inadama N, Murayama H, Omura T, et al. A depth of interaction detector for PET with GSO crystals doped with different amounts of Ce. IEEE Trans Nucl Sci 2002;49:629–33.
- [116] Fremout AAR, Chen R, Bruyndonckx P, et al. Spatial resolution and depth-of-interaction studies with a PET detector module composed of LSO and an APD array. IEEE Trans Nucl Sci 2002;49:131–8.
- [117] Shao Y, Silverman RW, Farrell R, et al. Design studies of a high resolution PET detector using APD arrays. IEEE Trans Nucl Sci 2000;47:1051–7.
- [118] Dokhale PA, Silverman RW, Shah KS, et al. Intrinsic spatial resolution and parallax correction using depth-encoding PET detector modules based on position-sensitive APD readout. IEEE Trans Nucl Sci 2006;53:2666–70.
- [119] Levin CS, Foudray AMK, Olcott PD, et al. Investigation of position sensitive avalanche photodiodes for a new high-resolution PET detector design. IEEE Trans Nucl Sci 2004;51:805–10.
- [120] Zhang J, Foudray AMK, Olcott PD, et al. Performance characterization of a novel thin position-sensitive avalanche photodiode for 1 mm resolution positron emission tomography. IEEE Trans Nucl Sci 2007;54:415–21.
- [121] Foudray AMK, Farrell R, Olcott PD, et al. Characterization of two thin position-sensitive avalanche photodiodes on a single flex circuit for use in 3-D positioning PET detectors. IEEE Nuclear Science Symposium Conference Record 2006;4:2469–72.
- [122] Levin CS, Matteson JL, Skelton RT, et al. Promising characteristics and performance of cadmium zinc telluride detectors for positron emission tomography. Presented at 2004 IEEE Nuclear Science Symp. and Medical Imaging Conf. Rome, Italy, October 16–22, 2004.

- Abstract no. M2-117, Book of Abstracts, p. 36. IEEE Nuclear and Plasma Science Society, 2004.
- [123] Levin CS, Foudray AM, Habte F. Impact of high energy resolution detectors on the performance of a PET system dedicated to breast cancer imaging. *Phys Med* 2006;21:28–34.
- [124] Chinn G, Foudray AMK, Levin CS. A method to include single photon events in image reconstruction for a 1 mm resolution PET system built with advanced 3-D positioning detectors. *IEEE Nuclear Science Symposium Conference Record* 2006;3:1740–5.
- [125] Chinn G, Foudray AMK, Levin CS. Accurately positioning and incorporating tissue-scattered photons into PET image reconstruction. *IEEE Nuclear Science Symposium Conference Record* 2006;3:1746–51.
- [126] Levin CS, Tai Y-C, Hoffman EJ, et al. Removal of the effect of Compton scattering in 3-D whole body positron emission tomography by Monte Carlo. *IEEE Nuclear Science Symposium and Medical Imaging Conference Record* 1995; 2:1050–4.
- [127] Ishii K, Kikuchi Y, Matsuyama S, et al. First achievement of less than 1 mm FWHM resolution in practical semiconductor animal PET scanner. *Nucl Instr Meth A* 2007;576:435–40.
- [128] Humm JL, Rosenfeld A, Del Guerra A. From PET detectors to PET scanners. *Eur J Nucl Med Mol Imaging* 2003;30:1574–97.
- [129] Zaidi H. Recent developments and future trends in nuclear medicine instrumentation. *Z Med Phys* 2006;16:5–17.
- [130] Levin CS. Application-specific small field-of-view imagers. In: Wernick M, Aarsvold J, editors. *Emission tomography: the fundamentals of PET and SPECT*. San Diego (CA): Academic Press; 2004. p. 293–334.
- [131] Slavis KR, Dowkontt PF, Duttweiler F, et al. Performance of a prototype CdZnTe detector module for hard x-ray astrophysics. In: Flanagan KA, Siegmund OHW, editors. *X-ray and gamma-ray instrumentation for astronomy XI*. San Diego (CA). 2000;4140:249–56.
- [132] Roberts RA, Barton BF. Theory of signal detectability: composite deferred decision theory, technical report No. 161. Michigan: University of Michigan; 1965.
- [133] Foudray AMK, Chinn C, Levin CS. Component based normalization for PET systems with depth of interaction measurement capability. In: *IEEE Nuclear Science Symposium Conference Record*. Puerto Rico: 2005. p. 23–9.
- [134] Rodriguez M, Barker WC, Liow JS, et al. Count-rate dependent component-based normalization for the HRRT [abstract]. *J Nucl Med* 2006;47 Supplement 1, Abstract Book, May 2006. p. 197P.
- [135] Leroux J-D, Selivanov V, Lecomte R, et al. Accelerated iterative image reconstruction methods based on block-circulant system matrix derived from a polar image representation. *IEEE Nuclear Science Symposium Conference Record* 2007. Piscataway, NJ. p. 3764–71.
- [136] Pratz G, Chinn G, Habte F, et al. Fully 3-D list-mode OSEM accelerated by graphics processing units. *IEEE Nuclear Science Symposium Conference Record* 2006;4:2196–202.
- [137] Xu F, Mueller K. Accelerating popular tomographic reconstruction algorithms on commodity PC graphics hardware. *IEEE Trans Nucl Sci* 2005;52:654–63.
- [138] Cabral B, Cam N, Foran J. Accelerated volume rendering and tomographic reconstruction using texture mapping hardware. In: Kaufman A, Krueger W, editors. *Proceedings of the 1994 symposium on volume visualization* 1994. p. 91–8.
- [139] Pratz G, Levin C. Accurately positioning events in a high-resolution PET system that uses 3D CZT detectors. In: *Proceedings of the IEEE Nuclear Science Symposium and Medical Imaging Conference* 2007. Piscataway, NJ. p. 2660–4.
- [140] Park JM, Gambhir SS. Multimodality radionuclide, fluorescence, and bioluminescence small-animal imaging. *Proceedings of the IEEE* 2005;93:771–83.
- [141] Maintz JB, Viergever MA. A survey of medical image registration. *Med Image Anal* 1998;2:1–36.
- [142] Pluim JP, Maintz JB, Viergever MA. Mutual-information-based registration of medical images: a survey. *IEEE Trans Med Imaging* 2003;22:986–1004.
- [143] Cross DJ, Minoshima S, Nishimura S, et al. Three-dimensional stereotactic surface projection analysis of macaque brain PET: development and initial applications. *J Nucl Med* 2000;41:1879–87.
- [144] Shimada Y, Uemura K, Ardekani BA, et al. Application of PET-MRI registration techniques to CAT brain imaging. *J Neurosci Methods* 2000;101:1–7.
- [145] Vaquero JJ, Desco M, Pascau J, et al. PET, CT, and MR image registration of the rat brain and skull. *IEEE Trans Nucl Sci* 2001;48: 1440–5.
- [146] Humm JL, Ballon D, Hu YC, et al. A stereotactic method for the three-dimensional registration of multi-modality biologic images in animals: NMR, PET, histology, and autoradiography. *Med Phys* 2003;30:2303–14.
- [147] Jan M-L, Chuang K-S, Chen G-W, et al. A three-dimensional registration method for automated fusion of micro PET-CT-SPECT whole-body images. *IEEE Trans Med Imaging* 2005;24:886–93.
- [148] Fei B, Wang H, Muzic J, et al. Deformable and rigid registration of MRI and microPET images for photodynamic therapy of cancer in mice. *Med Phys* 2006;33:753–60.
- [149] Deroose CM, De A, Loening AM, et al. Multi-modality imaging of tumor xenografts and

- metastases in mice with combined small-animal PET, small-animal CT, and bioluminescence imaging. *J Nucl Med* 2007; 48:295–303.
- [150] Slomka PJ. Software approach to merging molecular with anatomic information. *J Nucl Med* 2004;45:36S–45S.
- [151] Chow PL, Stout DB, Komisopoulou E, et al. A method of image registration for small animal, multi-modality imaging. *Phys Med Biol* 2006; 51:379–90.
- [152] Chow PL, Rannou FR, Chatzioannou AF. Attenuation correction for small animal PET tomographs. *Phys Med Biol* 2005;50:1837–50.
- [153] Hasegawa B, Zaidi H. Dual-modality imaging: more than the sum of its components. In: Zaidi H, editor. Quantitative analysis in nuclear medicine imaging. New York: Springer; 2006. p. 35–81.
- [154] Zavattini G, Vecchi S, Mitchell G, et al. A hyperspectral fluorescence system for 3D *in vivo* optical imaging. *Phys Med Biol* 2006;51: 2029–43.
- [155] Chaudhari AJ, Darvas F, Bading JR, et al. Hyperspectral and multispectral bioluminescence optical tomography for small animal imaging. *Phys Med Biol* 2005;50:5421–41.
- [156] Rannou FR, Kohli V, Prout DL, et al. Investigation of OPET performance using GATE, a Geant4-based simulation software. *IEEE Trans Nucl Sci* 2004;51:2713–7.
- [157] Alexandrakis G, Rannou FR, Chatzioannou AF. Tomographic bioluminescence imaging by use of a combined optical-PET (OPET) system: a computer simulation feasibility study. *Phys Med Biol* 2005;50:4225–41.
- [158] Gulsen G, Birgul O, Unlu MB, et al. Combined diffuse optical tomography (DOT) and MRI system for cancer imaging in small animals. *Technol Cancer Res Treat* 2006;5:351–63.
- [159] Farahani K, Slates R, Shao Y, et al. Contemporaneous positron emission tomography and MR imaging at 1.5 T. *J Magn Reson Imaging* 1999;9:497–500.
- [160] Slates R, Farahani K, Shao Y, et al. A study of artifacts in simultaneous PET and MR imaging using a prototype MR compatible PET scanner. *Phys Med Biol* 1999;44:2015–27.
- [161] Shao Y, Cherry SR, Farahani K, et al. Simultaneous PET and MR imaging. *Phys Med Biol* 1997;42:1965–70.
- [162] Mackewn JE, Strul D, Hallett WA, et al. Design and development of an MR-compatible PET scanner for imaging small animals. *IEEE Trans Nucl Sci* 2005;52:1376–80.
- [163] Pichler BJ, Judenhofer MS, Catana C, et al. Performance test of an LSO-APD detector in a 7-T MRI scanner for simultaneous PET/MRI. *J Nucl Med* 2006;47:639–47.
- [164] Lucas AJ, Hawkes RC, Ansorge RE, et al. Development of a combined microPET-MR system. *Technol Cancer Res Treat* 2006;5:337–41.
- [165] Judenhofer MS, Catana C, Swann BK, et al. Simultaneous PET/MR images, acquired with a compact MRI compatible PET detector in a 7 Tesla magnet. *Radiology* 2007;244:807–14.
- [166] Raylman RR, Majewski S, Lemieux SK, et al. Simultaneous MRI and PET imaging of a rat brain. *Phys Med Biol* 2006;51:6371–9.
- [167] Schlyer D, Rooney W, Woody C, et al. Development of a simultaneous PET/MRI scanner. In: Seibert JA, editor. Proceedings of the IEEE Nuclear Science Symposium Conference Record. Rome (Italy): October 19–22, 2004. p. 3419–21.
- [168] Yamamoto S, Takamatsu S, Murayama H, et al. A block detector for a multislice, depth-of-interaction MR-compatible PET. *EEE Trans Nucl Sci* 2005;52:33–7.
- [169] Marsden PK, Strul D, Keevil SF, et al. Simultaneous PET and NMR. *Br J Radiol* 2002;75:S53–9.
- [170] Catana C, Wu Y, Judenhofer MS, et al. Simultaneous acquisition of multislice PET and MR images: initial results with a MR-compatible PET scanner. *J Nucl Med* 2006;47:1968–76.
- [171] Peter J, Semmler W. A modular design triple-modality SPECT-CT-ODT small animal imager. [abstract]. *Eur J Nucl Med Mol Imaging* 2007; 34:S158.
- [172] Meikle SR, Kench P, Kassiou M, et al. Small animal SPECT and its place in the matrix of molecular imaging technologies. *Phys Med Biol* 2005;50:R45–61.
- [173] Beekman F, Have Fvd. The pinhole: gateway to ultra-high-resolution three-dimensional radio-nuclide imaging. *Eur J Nucl Med Mol Imaging* 2007;V34:151–61.
- [174] Kim H, Furenlid LR, Crawford MJ, et al. Semi-SPECT: a small-animal single-photon emission computed tomography (SPECT) imager based on eight cadmium zinc telluride (CZT) detector arrays. *Med Phys* 2006;33:465–74.
- [175] Goertzen AL, Jones DW, Seidel J, et al. First results from the high-resolution mouseSPECT annular scintillation camera. *IEEE Trans Med Imaging* 2005;24:863–7.
- [176] Patt B, Parnham K, Li J, et al. FLEX: tri-modality small animal tomography combining PET, SPECT and CT in a single modular gantry. [abstract]. *J Nucl Med* 2005;46:207P.
- [177] Saoudi A, Lecomte R. A novel APD-based detector module for multi-modality PET/SPECT/CT scanners. *IEEE Trans Nucl Sci* 1999;46:479–84.
- [178] Goertzen AL, Meadors AK, Silverman RW, et al. Simultaneous molecular and anatomical imaging of the mouse *in vivo*. *Phys Med Biol* 2002;47:4315–28.
- [179] Bérard P, Riendeau J, Pepin C, et al. Investigation of the LabPET detector and electronics for photon-counting CT imaging. *Nucl Instr Meth A* 2007;571:114–7.
- [180] Liang H, Yang Y, Yang K, et al. A microPET/CT system for *in vivo* small animal imaging. *Phys Med Biol* 2007;52:3881–94.

- [181] Kiessling F, Greschus S, Lichy MP, et al. Volumetric computed tomography (VCT): a new technology for noninvasive, high-resolution monitoring of tumor angiogenesis. *Nat Med* 2004;10:1133–8.
- [182] Andre MP, Spivey BA, Martin PJ, et al. Integrated CMOS-selenium x-ray detector for digital mammography. *Proc SPIE* 1998;3336:204–9.
- [183] Yang Y, Tai YC, Siegel S, et al. Optimization and performance evaluation of the microPET II scanner for in vivo small-animal imaging. *Phys Med Biol* 2004;49:2527–45.
- [184] Prout DL, Silverman RW, Chatzioannou A. Detector concept for OPET-A combined PET and optical imaging system. *IEEE Trans Nucl Sci* 2004;51:752–6.
- [185] Alexandrakis G, Rannou FR, Chatzioannou AF. Effect of optical property estimation accuracy on tomographic bioluminescence imaging: simulation of a combined optical-PET (OPET) system. *Phys Med Biol* 2006;51:2045–53.
- [186] Prout DL, Silverman RW, Chatzioannou A. Readout of the optical PET (OPET) detector. *IEEE Trans Nucl Sci* 2005;52:28–32.
- [187] Peter J, Semmler W. vECTlab—a fully integrated multi-modality Monte Carlo simulation framework for the radiological imaging sciences. *Nucl Instr Meth A* 2007;580:955–9.
- [188] Hammer BE, Christensen NL, Heil BG. Use of a magnetic field to increase the spatial resolution of positron emission tomography. *Med Phys* 1994;21:1917–20.
- [189] Christensen NL, Hammer BE, Heil BG, et al. Positron emission tomography within a magnetic field using photomultiplier tubes and light-guides. *Phys Med Biol* 1995;40:691–7.
- [190] Raylman RR, Hammer BE, Christensen NL. Combined MRI-PET scanner: a Monte-Carlo evaluation of the improvements in PET resolution due to the effects of a static homogeneous magnetic field. *IEEE Trans Nucl Sci* 1996;43:2406–12.
- [191] Garlick PB. Simultaneous PET and NMR-Initial results from isolated, perfused rat hearts. *Br J Radiol* 2002;75:S60–6.
- [192] Garlick PB, Marsden PK, Cave AC, et al. PET and NMR dual acquisition (PANDA): applications to isolated perfused rat hearts. *NMR Biomed* 1997;10:138–42.
- [193] Zaidi H, Alavi A. Current trends in PET and combined (PET/CT and PET/MR) systems design. *PET Clinics* 2(2); in press.
- [194] Raylman RR, Majewski S, Velan SS, et al. Simultaneous acquisition of magnetic resonance spectroscopy (MRS) data and positron emission tomography (PET) images with a prototype MR-compatible, small animal PET imager. *J Magn Reson* 2007;186:305–10.
- [195] Handler WB, Gilbert KM, Peng H, et al. Simulation of scattering and attenuation of 511 keV photons in a combined PET/field-cycled MRI system. *Phys Med Biol* 2006;51:2479–91.
- [196] Dolgoshein B, Balagura V, Buzhan P, et al. Status report on silicon photomultiplier development and its applications. *Nucl Instr Meth A* 2006;563:368–76.
- [197] Moehrs S, Del Guerra A, Herbert DJ, et al. A detector head design for small-animal PET with silicon photomultipliers (SiPM). *Phys Med Biol* 2006;51:1113–27.
- [198] Judenhofer MS, Wehrli HF, Newport DF, et al. Simultaneous PET/MRI: a new perspective for functional and morphological imaging. *Nat Med* 2008; in press.
- [199] Vaska P, Woody CL, Schlyer DJ, et al. RatCAP: miniaturized head-mounted PET for conscious rodent brain imaging. *IEEE Trans Nucl Sci* 2004;51:2718–22.
- [200] Woody C, Schlyer D, Vaska P, et al. Preliminary studies of a simultaneous PET/MRI scanner based on the RatCAP small animal tomograph. *Nucl Instr Meth A* 2007;571:102–5.
- [201] Zaidi H, Mawlawi O, Orton CG. Point/counterpoint. Simultaneous PET/MR will replace PET/CT as the molecular multimodality imaging platform of choice. *Med Phys* 2007;34:1525–8.
- [202] Acton PD, Zhuang H, Alavi A. Quantification in PET. *Radiol Clin North Am* 2004;42:1055–62.
- [203] Convert L, Morin-Brassard G, Cadorette J, et al. A new tool for molecular imaging: the microvolumetric $\{\beta\}$ blood counter. *J Nucl Med* 2007;48:1197–206.
- [204] Wu HM, Sui G, Lee CC, et al. In vivo quantitation of glucose metabolism in mice using small-animal PET and a microfluidic device. *J Nucl Med* 2007;48:837–45.
- [205] Meyer PT, Circiumaru V, Cardi CA, et al. Simplified quantification of small animal [18F]FDG PET studies using a standard arterial input function. *Eur J Nucl Med Mol Imaging* 2006;33:948–54.
- [206] Bentourkia M, Zaidi H. Tracer kinetic modeling in PET. *PET Clinics* 2(2); in press.
- [207] Torres-Espallardo I, Spanoudaki VC, Rafecas M, et al. Quantification issues in imaging data of MADPET-II small animal scanner using a system matrix based on Monte Carlo techniques. In: Proceedings of the IEEE Nuclear Science Symposium and Medical Imaging Conference, Record 2007. Piscataway, NJ. p. 4192–7.
- [208] Zaidi H, Montandon M, Alavi A. Attenuation correction techniques in PET. *PET Clinics* 2(2); in press.
- [209] Rahmim A, Rousset OG, Zaidi H. Strategies for motion tracking and correction in PET. *PET Clinics* 2(2); in press.
- [210] Fueger BJ, Czernin J, Hildebrandt I, et al. Impact of animal handling on the results of 18F-FDG PET studies in mice. *J Nucl Med* 2006;47:999–1006.
- [211] Hideo T, Nishiyama S, Kakiuchi T, et al. Ketamine alters the availability of striatal dopamine transporter by [11C] β -CFT and

- [21C] β -CIT-FE in the monkey brain. *Synapse* 2001;42:273–80.
- [212] Jagoda EM, Vaquero JJ, Seidel J, et al. Experiment assessment of mass effects in the rat: implications for small animal PET imaging. *Nucl Med Biol* 2004;31:771–9.
- [213] Toyama H, Ichise M, Liow JS, et al. Absolute quantification of regional cerebral glucose utilization in mice by 18F-FDG small animal PET scanning and 2-14C-DG autoradiography. *J Nucl Med* 2004;45:1398–405.
- [214] Fahey FH, Gage HD, Buchheimer N, et al. Evaluation of the quantitative capability of a high-resolution positron emission tomography scanner for small animal imaging. *J Comput Assist Tomogr* 2004;28:842–8.
- [215] Kesner AL, Dahlbom M, Huang SC, et al. Semiautomated analysis of small-animal PET data. *J Nucl Med* 2006;47:1181–6.
- [216] Aide N, Louis MH, Dutoit S, et al. Improvement of semi-quantitative small-animal PET data with recovery coefficients: a phantom and rat study. *Nucl Med Commun* 2007;28:813–22.
- [217] Vaska P, Rubins DJ, Alexoff DL, et al. Quantitative imaging with the micro-PET small-animal PET tomograph. *Int Rev Neurobiol* 2006;73:191–218.
- [218] Casteels C, Vermaelen P, Nuyts J, et al. Construction and evaluation of multitracer small-animal PET probabilistic atlases for voxel-based functional mapping of the rat brain. *J Nucl Med* 2006;47:1858–66.
- [219] Rubins DJ, Melega WP, Lacan G, et al. Development and evaluation of an automated atlas-based image analysis method for microPET studies of the rat brain. *Neuroimage* 2003;20:2100–18.
- [220] Segars WP, Tsui BM, Frey EC, et al. Development of a 4-D digital mouse phantom for molecular imaging research. *Mol Imaging Biol* 2004;6:149–59.
- [221] Beekman FJ, Vastenhoud B. Design and simulation of a high-resolution stationary SPECT system for small animals. *Phys Med Biol* 2004;49:4579–92.
- [222] Dogdas B, Stout D, Chatzioannou AF, et al. Digimouse: a 3D whole body mouse atlas from CT and cryosection data. *Phys Med Biol* 2007;52:577–87.
- [223] Taschereau R, Chow PL, Chatzioannou AF. Monte Carlo simulations of dose from microCT imaging procedures in a realistic mouse phantom. *Med Phys* 2006;33:216–24.
- [224] Stabin MG, Peterson TE, Holburn GE, et al. Voxel-based mouse and rat models for internal dose calculations. *J Nucl Med* 2006;47:655–9.
- [225] Zaidi H, Xu XG. Computational anthropomorphic models of the human anatomy: the path to realistic Monte Carlo modeling in medical imaging. *Annu Rev Biomed Eng* 2007;9:471–500.
- [226] Hichwa R. Are animal scanners really necessary for PET? *J Nucl Med* 1994;35:1396–7.
- [227] Tornai MP, Jaszcza RJ, Turkington TG, et al. Small-animal PET: advent of a new era of PET research. *J Nucl Med* 1999;40:1176–9.
- [228] Nanni C, Rubello D, Fanti S. Role of small animal PET for molecular imaging in pre-clinical studies. *Eur J Nucl Med Mol Imaging* 2007;34:1819–22.
- [229] Tatsumi M, Nakamoto Y, Traughber B, et al. Initial experience in small animal tumor imaging with a clinical positron emission tomography/computed tomography scanner using 2-[F-18]Fluoro-2-deoxy-D-glucose. *Cancer Res* 2003;63:6252–7.
- [230] Seemann MD, Beck R, Ziegler S. In vivo tumor imaging in mice using a state-of-the-art clinical PET/CT in comparison with a small animal PET and a small animal CT. *Technol Cancer Res Treat* 2006;5:537–42.
- [231] Nanni C, Rubello D, Khan S, et al. Role of small animal PET in stimulating the development of new radiopharmaceuticals in oncology. *Nucl Med Commun* 2007;28:427–9.
- [232] Wester H-J. Nuclear imaging probes: from bench to bedside. *Clin Cancer Res* 2007;13:3470–81.
- [233] Aboagye EO. Positron emission tomography imaging of small animals in anticancer drug development. *Mol Imaging Biol* 2005;7:53–8.
- [234] Richter W. Imaging biomarkers as surrogate endpoints for drug development. *Eur J Nucl Med Mol Imaging* 2006;33:6–10.
- [235] Pien HH, Fischman AJ, Thrall JH, et al. Using imaging biomarkers to accelerate drug development and clinical trials. *Drug Discov Today* 2005;10:259–66.
- [236] Lucignani G. Imaging biomarkers: from research to patient care—a shift in view. *Eur J Nucl Med Mol Imaging* 2007;34:1693–7.
- [237] Stephen R, Gillies R. Promise and progress for functional and molecular imaging of response to targeted therapies. *Pharm Res* 2007;24:1172–85.
- [238] Czernin J, Weber WA, Herschman HR. Molecular imaging in the development of cancer therapeutics. *Annu Rev Med* 2006;57:99–118.
- [239] Cherry SR, Gambhir S. Use of positron emission tomography in animal research. *Inst Lab Animal Res* 2001;42:219–32.
- [240] Hanahan D. Transgenic mice as probes into complex systems. *Science* 1989;246:1265–75.
- [241] Torigian DA, Huang SS, Houseni M, et al. Functional imaging of cancer with emphasis on molecular techniques. *CA Cancer J Clin* 2007;57:206–24.
- [242] Shmidt EN, Nitkin AY. Pathology of mouse models of human lung cancer. *Comp Med* 2004;54:23–6.
- [243] Kwak L, Tsai SY, DeMayo FJ. Genetically engineered mouse models for lung cancer. *Annu Rev Physiol* 2004;66:647–63.

- [244] Janssen KP. Murine models of colorectal cancer: studying the role of oncogenic K-ras. *Cell Mol Life Sci* 2003;60:495–506.
- [245] Boivin GP, Groden J. Mouse models of intestinal cancer. *Comp Med* 2004;54:15–8.
- [246] Dyer MA. Mouse models of childhood cancer of the nervous system. *Journal of Clin Pathology* 2004;57:561–76.
- [247] Mant C, Cason J. A human murine mammary tumour virus-like agent is an unconvincing aetiological agent for human breast cancer. *Rev Med Virol* 2004;14:169–77.
- [248] Gravkamp C, Sypniewska R, Hoflack L. The usefulness of mouse breast tumor models for testing and optimization of breast cancer vaccines at old age. *Mech Ageing Dev* 2004;125:125–7.
- [249] Bursch W, Grasl-Kraupp B, Wastl U, et al. Role of apoptosis for mouse liver growth regulation and tumor promotion: comparative analysis of mice with high (C3H/He) and low (C57Bl/6J) cancer susceptibility. *Toxicol Lett* 2004;149:25–35.
- [250] Shappell SB, Thomas GV, Roberts RL, et al. Prostate pathology of genetically engineered mice: definitions and classification. The consensus report from the Bar Harbor meeting of the Mouse Models of Human Cancer Consortium Prostate Pathology Committee. *Cancer Res* 2004;64:2270–305.
- [251] Garrison JC, Rold TL, Sieckman GL, et al. In vivo evaluation and small-animal PET/CT of a prostate cancer mouse model using ⁶⁴Cu bombesin analogs: side-by-side comparison of the CB-TE2A and DOTA chelation systems. *J Nucl Med* 2007;48:1327–37.
- [252] Leach SD. Mouse models of pancreatic cancer: the fur is finally flying! *Cancer Cell* 2004;5:7–11.
- [253] Arbeit JM. Mouse models of cervical cancer. *Comp Med* 2003;53:256–8.
- [254] James JF, Hewett TE, Robbins J. Cardiac physiology in transgenic mice. *Circ Res* 1998;82:407–15.
- [255] Bader M, Bohnemeier H, Zollmann FS, et al. Transgenic animals in cardiovascular disease research. *Exp Physiol* 2000;85:713–31.
- [256] Kreissl MC, Wu HM, Stout DB, et al. Noninvasive measurement of cardiovascular function in mice with high-temporal-resolution small-animal PET. *J Nucl Med* 2006;47:974–80.
- [257] Lavoie JL, Bianco RA, Sakai K, et al. Transgenic mice for studies of the renin-angiotensin system in hypertension. *Acta Physiol Scand* 2004;181:571–7.
- [258] Janssen BJ, Smits JF. Autonomic control of blood pressure in mice: basic physiology and effects of genetic modification. *Am J Physiol Regul Integr Comp Physiol* 2002;282:R1545–64.
- [259] Gros D, Dupays L, Alcolea S, et al. Genetically modified mice: tools to decode the functions of connexins in the heart-new models for cardiovascular research. *Cardiovasc Res* 2004;62:299–308.
- [260] Wessels A, Phelps A, Trusk TC, et al. Mouse models for cardiac conduction system development. *Novartis Found Symp* 2003;250:44–59 [discussion: 59–67 and 276–9].
- [261] Russo GL, Russo M. Ins and outs of apoptosis in cardiovascular diseases. *Nutr Metab Cardiovasc Dis* 2003;13:291–300.
- [262] Bernstein D. Exercise assessment of transgenic models of human cardiovascular disease. *Physiol Genomics* 2003;13:217–26.
- [263] Fruchart JC, Duriez P. High density lipoproteins and coronary heart disease. Future prospects in gene therapy. *Biochimie* 1998;80:167–72.
- [264] Kopecky J, Flachs P, Bardova K, et al. Modulation of lipid metabolism by energy status of adipocytes: implications for insulin sensitivity. *Ann N Y Acad Sci* 2002;967:88–101.
- [265] Carmeliet P, Collen D. Transgenic mouse models in angiogenesis and cardiovascular disease. *J Pathol* 2000;190:387–405.
- [266] Daugherty A. Mouse models of atherosclerosis. *Am J Med Sci* 2002;323:3–10.
- [267] Rossin R, Berndorff D, Friebe M, et al. Small-animal PET of tumor angiogenesis using a (76)Br-labeled human recombinant antibody fragment to the ED-B domain of fibronectin. *J Nucl Med* 2007;48:1172–9.
- [268] Jacobs AH, Li H, Winkeler A, et al. PET-based molecular imaging in neuroscience. *Eur J Nucl Med Mol Imaging* 2003;30:1051–65.
- [269] Bernstein A, Breitman M. Genetic ablation in transgenic mice. *Mol Biol Med* 1989;6:523–30.
- [270] Doetschman T. Interpretation of phenotype in genetically engineered mice. *Lab Anim Sci* 1999;49:137–43.
- [271] Funk T, Sun M, Hasegawa BH. Radiation dose estimate in small animal SPECT and PET. *Med Phys* 2004;31:2680–6.
- [272] Taschereau R, Chatzilooannou AF. Monte Carlo simulations of absorbed dose in a mouse phantom from 18-fluorine compounds. *Med Phys* 2007;34:1026–36.
- [273] Hindorf C, Ljungberg M, Strand SE. Evaluation of parameters influencing S values in mouse dosimetry. *J Nucl Med* 2004;45:1960–5.